Advancing Palladium-Based Nanostructures for Catalysis

From Nanoparticles to Multifunctional Nanoarchitectures

Bermeo Vargas, Marie

2025

Document Version:
Publisher's PDF, also known as Version of record

Advancing Palladium-Based Nanostructures for Catalysis

From Nanoparticles to Multifunctional Nanoarchitectures

MARIE PRISCILA BERMEO VARGAS
DEPARTMENT OF PHYSICS | FACULTY OF ENGINEERING | LUND UNIVERSITY

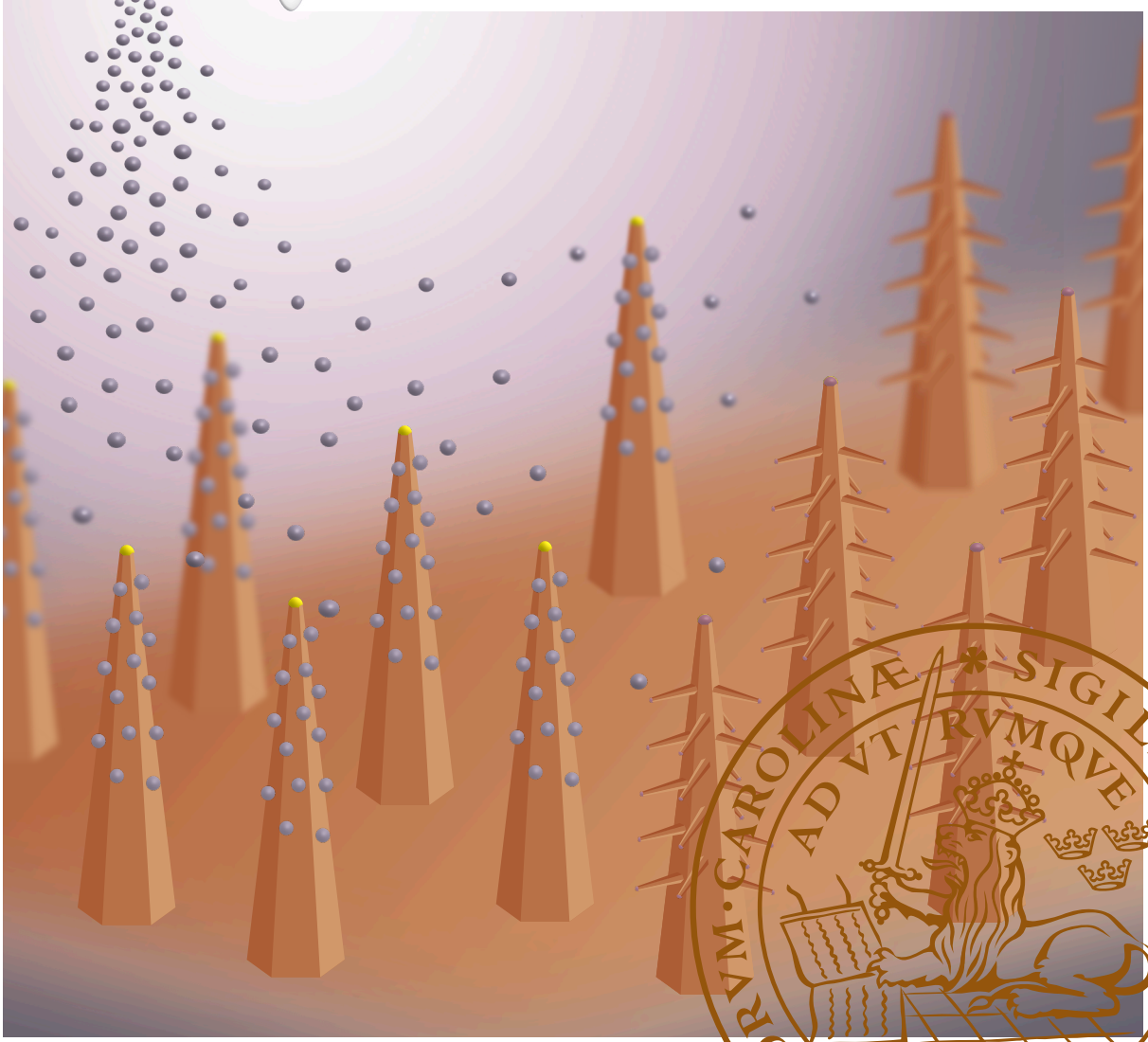

A day in Nanolund, operating the MOVPE- Aixtron CCS to grow nanowires.

Printed by Media-Tryck, Lund 2025 NORDIC SWAN ECOLABEL 3041 0903

LUND UNIVERSITY

Faculty of Engineering
Department of Physics

ISBN 978-91-8104-465-2

Advancing Palladium-Based Nanostructures for Catalysis:

From Nanoparticles to Multifunctional Nanoarchitectures.

Advancing Palladium-Based Nanostructures for Catalysis:

From Nanoparticles to Multifunctional Nanoarchitectures

Marie Priscila Bermeo Vargas

LUND
UNIVERSITY

DOCTORAL THESIS

To be publicly defended, with the permission of the Faculty of Engineering, Lund University, on Friday, the 25th of April 2025, at 09.15 in the Rydberg Lecture Hall (Rydbergsalen) at the Department of Physics

Thesis advisors
Maria E. Messing, Martin H. Magnusson, and Sara Blomberg

Faculty opponent
Prof. Lutz Mädler
Universität Bremen, Germany

Organisation: LUND UNIVERSITY	**Document name:** DOCTORAL DISSERTATION	
	Date of disputation: April 25, 2025	
Author: Marie Priscila Bermeo Vargas	**Sponsoring organisation:**	

Title: Advancing Palladium-Based Nanostructures for Catalysis: From Nanoparticles to Multifunctional Nanoarchitectures

Abstract

The development of nanoscale materials is essential across various fields, including catalysis. The intrinsic properties of well-defined nanometre-sized catalysts directly influence their catalytic performance. This thesis investigates the design, fabrication and optimisation of palladium (Pd)-based nanostructures as potential nanocatalysts through a multidisciplinary approach combining state-of-the-art fabrication and characterisation methods.

High-purity Pd nanoparticles, fabricated via a chemical-free spark ablation method, serve as the core building blocks, offering precise control over size and composition, essential for tuneable catalytic properties.

The first study, addressed in Paper I, focuses on enhancing spark discharge generator (SDG) efficiency through COMSOL simulations and experimental studies, paving the way for higher-throughput catalytic nanoparticle production.

The nanoparticle tunability extended to Pd-based alloys was investigated in Paper II, exploring the synthesis of Pd-Ga alloy nanoparticles via a novel combination of spark ablation and in-flight metal-organic precursor decomposition, which demonstrates the ability to fine-tune catalytic properties by controlling composition and processing conditions.

Pd nanoparticles are further integrated with gallium phosphide (GaP) nanowires to create innovative hybrid nanocatalysts, as detailed in Paper III. The design and surface engineering of these nanostructures reveal the critical role of their morphology in catalytic performance, particularly in hydrogenation reactions.

The final study, in Paper IV, examines the growth of branched GaP nanowires using Pd nanoparticles as seeds, achieving three-dimensional structures with enhanced surface area and attractive for catalytic applications.

This research contributes to the development of solid-state nanocatalysts by leveraging the precise generation of Pd nanoparticles and alloy materials and their integration with semiconductor-based supports. The findings highlight the potential for these materials as nanocatalysts.

Key words: Nanoparticles, spark ablation, nanowires, palladium, gallium phosphide, catalysis

Classification system and/or index terms (if any)

Supplementary bibliographical information — **Language:** English

ISSN and key title: — **ISBN:** 978-91-8104-465-2 (print) 978-91-8104-466-9 (pdf)

Recipient's notes — **Number of pages:** 117 — Price

Security classification

Advancing Palladium-Based Nanostructures for Catalysis:

From Nanoparticles to Multifunctional Nanoarchitectures

Marie Priscila Bermeo Vargas

LUND
UNIVERSITY

Front cover by Marie P. Bermeo Vargas

Faculty
Department

ISBN 978-91-8104-465-2 (print)
ISSN 978-91-8104-466-9 (pdf)

Printed in Sweden by Media-Tryck, Lund University
Lund 2025

Dedicated to my family: My parents, Santiago and Flor,
and siblings, Cristina, Pavell, Ekaterina, and Elias

Table of Contents

Abstract

The development of nanoscale materials is essential across various fields, including catalysis. The intrinsic properties of well-defined nanometre-sized catalysts directly influence their catalytic performance. This thesis investigates the design, fabrication and optimisation of palladium (Pd)-based nanostructures as potential nanocatalysts through a multidisciplinary approach combining state-of-the-art fabrication and characterisation methods.

High-purity Pd nanoparticles, fabricated via a chemical-free spark ablation method, serve as the core building blocks, offering precise control over size and composition, essential for tuneable catalytic properties.

The first study, addressed in Paper I, focuses on enhancing spark discharge generator (SDG) efficiency through COMSOL simulations and experimental studies, paving the way for higher-throughput catalytic nanoparticle production.

The nanoparticle tunability extended to Pd-based alloys was investigated in Paper II, exploring the synthesis of Pd-Ga alloy nanoparticles via a novel combination of spark ablation and in-flight metal-organic precursor decomposition, which demonstrates the ability to fine-tune catalytic properties by controlling composition and processing conditions.

Pd nanoparticles are further integrated with gallium phosphide (GaP) nanowires to create innovative hybrid nanocatalysts, as detailed in Paper III. The design and surface engineering of these nanostructures reveal the critical role of their morphology in catalytic performance, particularly in hydrogenation reactions.

The final study, in Paper IV, examines the growth of branched GaP nanowires using Pd nanoparticles as seeds, achieving three-dimensional structures with enhanced surface area and attractive for catalytic applications.

This research contributes to the development of solid-state nanocatalysts by leveraging the precise generation of Pd nanoparticles and alloy materials and their integration with semiconductor-based supports. The findings highlight the potential for these materials as nanocatalysts.

Popular Science

Advancing nanostructures: palladium nanoparticles and beyond

Scientists are engineering materials at scales smaller than one billionth of a meter. That's about a thousand times thinner than a human hair! These tiny materials are invisible to the naked eye. They can be produced in different shapes, compositions, and architectures, enabling unprecedented control over their properties and functionality - all thanks to the fascinating realm of nanotechnology, where incredible possibilities emerge.

At this minuscule level, these so-called nanomaterials behave in extraordinary ways, opening doors to innovations that seemed like science fiction just a few decades ago. One of the most exciting frontiers in this nano-world is the development of nanocatalysts—tiny powerhouses that supercharge chemical reactions with applications spanning medicine, food production, and sustainable energy.

A promising advance in this domain involves combining the unique properties of palladium (Pd) nanoparticles with support nanostructures such as pedestalled gallium phosphide (GaP) nanowires. Let us dive into how this innovation may influence the future of catalysis.

The role of nanocatalysts

Catalysts are substances that accelerate chemical reactions without being consumed in the process. The advent of nanotechnology has added a new dimension to catalysis by introducing nanocatalysts, which offer a combination of high surface area and unique surface properties due to their nanoscale dimensions. This high surface-to-volume ratio ensures more reactive sites, enhancing reaction efficiency.

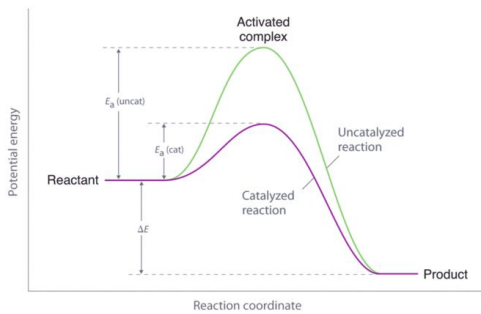

Pd, a precious metal, is a star player in the field of catalysis. Known for its exceptional ability to activate and break chemical bonds, Pd is widely used in the production of high-quality fuels, drug compounds, automotive catalytic converters, and fuel cell technologies. However, its limited availability and high cost have driven researchers to optimise its use through nanotechnology.

The journey begins: spark ablation to produce palladium nanoparticles

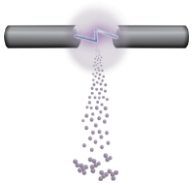

One innovative method to produce Pd nanoparticles is spark ablation, a chemical reagent-free process that generates high-purity nanoparticles. In this technique, a high-voltage electrical spark is discharged between two electrodes made of Pd. The energy from the spark vaporises the metal, and the resulting vapour condenses into Pd nanoparticles.

What makes spark ablation particularly exciting is its versatility since it is possible to easily control the composition, size, and concentration of the nanoparticles, allowing customisation of their properties for different applications.

Exploring alloys: palladium-gallium compounds

The properties of pure Pd nanoparticles can be enhanced by producing Pd-based alloys. Among diverse options, Pd-Ga alloy nanoparticles combine Pd's advantageous catalytic activity with Ga's unique properties. Using spark ablation combined with in-flight decomposition of a precursor of Ga, it is possible to synthesise Pd-Ga nanoparticles with tuneable compositions.

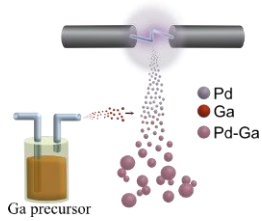

The ability to produce these alloys offers exciting opportunities for applications requiring specific catalytic properties. For instance, Pd-Ga nanoparticles have shown promise in reactions to produce methanol from CO_2, which is of great interest to sustainable energy applications.

Bridging dimensions: gallium phosphide nanowires as supports

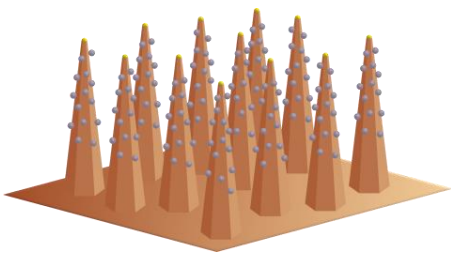

An innovative approach to designing Pd-based nanocatalysts combines Pd nanoparticles with supportive structures that enhance their stability and accessibility. Pedestalled GaP nanowires—tiny rod-like structures—are ideal candidates. GaP is a biocompatible semiconductor material with good thermal and chemical stability, making it an excellent support for Pd-based catalysts. The one-dimensional nanowire structures provide an expansive surface area, allowing for more extensive interaction between the Pd nanoparticles and the reactants.

3D nanostructures: nanotrees

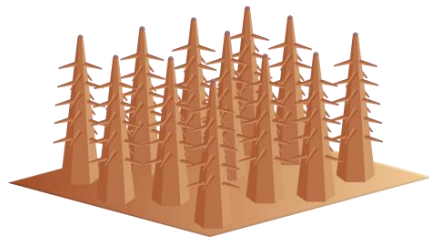

The good synergy between Pd and Ga takes this nanocatalyst concept further by decorating GaP nanowires with a second batch of Pd nanoparticles and growing branches from the core GaP nanowires. Such 3D nanostructures, resembling nanotrees, provide an extended surface area and form Pd-Ga phases at the branch tips, which are helpful for catalytic applications. These complex nanoarchitectures promise enhanced performance in catalytic reactions due to their increased active sites and the Pd-Ga synergy.

Influencing the future of nanostructures for catalysis: This thesis

The journey of Pd-based nanostructures for catalysis is far from over. As researchers, we continue pushing the boundaries of what is possible at the nanoscale, exploring new ways to optimise properties and develop amazing nanoarchitectures.

This thesis unveils the intricate details of how these Pd-based nanocatalysts were designed, fabricated, and tested. Let's take a closer look at the exciting journey it presents.

This work starts with Pd nanoparticle generation through spark ablation and exploring the effects of various chamber configurations on nanoparticle output via simulations and experimental measurements. A further step was demonstrating the production of Pd-Ga alloys and the identification of several phase formations with varying operating conditions. Afterwards, an innovative design and fabrication of semiconductor nanowires decorated with Pd nanoparticles resulted in several nanocatalysts being evaluated and tested for catalysis and, finally, advancing the nanocatalyst architectures by fabricating branched GaP nanowires, creating tree-like structures at the nanoscale.

Divulgación científica

Avance en nanoestructuras: nanopartículas de paladio y más

Los científicos están diseñando materiales a escalas menores a una milmillonésima de metro. ¡Eso es unas mil veces más delgado que un cabello humano! Estos materiales diminutos son invisibles al ojo humano. Se pueden producir en diferentes formas, composiciones y arquitecturas, permitiendo un control sin precedentes sobre sus propiedades y funcionalidad - todo gracias al fascinante mundo de la nanotecnología, donde surgen posibilidades increíbles.

A este nivel minúsculo, estos llamados nanomateriales se comportan de maneras extraordinarias, abriendo puertas a innovaciones que parecían ciencia ficción hace solo unas décadas. Una de las fronteras más emocionantes en este nano-mundo es el desarrollo de nanocatalizadores—diminutas centrales de energía que potencian las reacciones químicas con aplicaciones que abarcan la medicina, la producción de alimentos y la energía sostenible.

Un avance prometedor en este campo implica combinar las propiedades únicas de las nanopartículas de paladio (Pd) con nanoestructuras de soporte como nanohilos de fosfuro de galio (GaP) con pedestal. Sumerjámonos en cómo esta innovación puede influir en el futuro de la catálisis.

El Papel de los nanocatalizadores

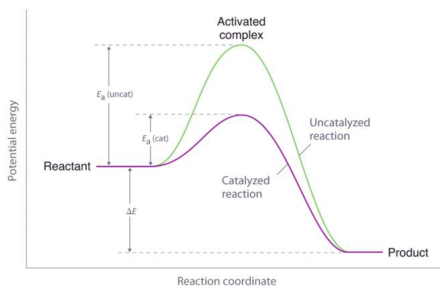

Los catalizadores son sustancias que aceleran las reacciones químicas sin ser consumidas en el proceso. El advenimiento de la nanotecnología ha añadido una nueva dimensión a la catálisis introduciendo nanocatalizadores, que ofrecen una combinación de alta área y propiedades superficiales únicas debido a sus dimensiones nanométricas. Esta alta relación superficie-volumen asegura más sitios reactivos, mejorando la eficiencia de la reacción.

El Pd, un metal precioso, es una estrella en el campo de la catálisis. Conocido por su excepcional capacidad para activar y romper enlaces químicos, el Pd se utiliza ampliamente en la producción de combustibles de alta calidad, compuestos farmacéuticos, convertidores catalíticos para automóviles y tecnologías de celdas de combustible. Sin embargo, su disponibilidad limitada y alto costo han llevado a los investigadores a optimizar su uso a través de la nanotecnología.

El viaje comienza: ablación por chispa para nanopartículas de paladio

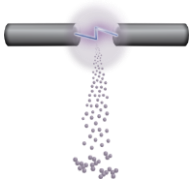

Un método innovador para producir nanopartículas de Pd es la ablación por chispa, un proceso libre de reactivos químicos que genera nanopartículas de alta pureza. En esta técnica, se descarga una chispa eléctrica de alto voltaje entre dos electrodos hechos de Pd. La energía de la chispa vaporiza el metal, y el vapor resultante se condensa en nanopartículas de Pd.

Lo que hace particularmente emocionante la ablación por chispa es su versatilidad, ya que es posible controlar fácilmente la composición, el tamaño y la concentración de las nanopartículas, permitiendo personalizar sus propiedades para diferentes aplicaciones.

Explorando aleaciones: compuestos de paladio-galio

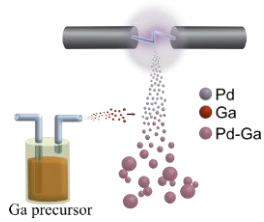

Las propiedades de las nanopartículas de Pd puro pueden mejorarse produciendo aleaciones basadas en Pd. Entre diversas opciones, las nanopartículas de aleación Pd-Ga combinan la ventajosa actividad catalítica del Pd con las propiedades únicas del Ga. Utilizando ablación por chispa combinada con descomposición en vuelo de un precursor de Ga, es posible sintetizar nanopartículas de Pd-Ga con composiciones ajustables.

La capacidad de producir estas aleaciones ofrece oportunidades emocionantes para aplicaciones que requieren propiedades catalíticas específicas. Por ejemplo, las nanopartículas de Pd-Ga han mostrado promesa en reacciones para producir metanol a partir de CO_2, lo cual es de gran interés para aplicaciones de energía sostenible.

Conectando dimensiones: nanohilos de fosfuro de galio como soportes

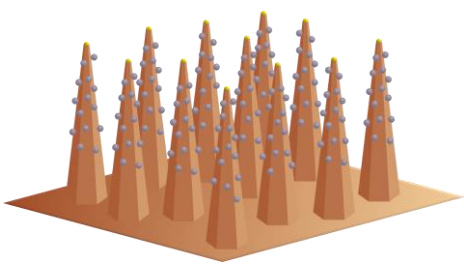

Un enfoque innovador para diseñar nanocatalizadores basados en Pd combina nanopartículas de Pd con estructuras de soporte que mejoran su estabilidad y accesibilidad. Los nanohilos de GaP con pedestal—pequeñas estructuras en forma de varilla—son candidatos ideales. El GaP es un material semiconductor biocompatible con buena estabilidad térmica y química, lo que lo convierte en un excelente soporte para catalizadores basados en Pd. Las estructuras unidimensionales de nanohilos proporcionan un área superficial expansiva, permitiendo una interacción más extensa entre las nanopartículas de Pd y los reactivos.

Nanoestructuras 3D: nanoárboles

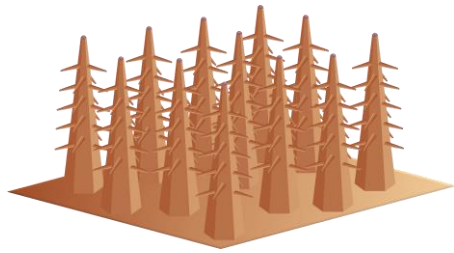

La buena sinergia entre Pd y Ga lleva este concepto de nanocatalizador más allá al decorar nanohilos de GaP con un segundo lote de nanopartículas de Pd y hacer crecer ramas desde los nanohilos de GaP. Tales nanoestructuras 3D, que se asemejan a nanoárboles, proporcionan un área superficial extendida y forman fases Pd-Ga en las puntas de las ramas, que son útiles para aplicaciones catalíticas. Estas nanoarquitecturas complejas prometen un rendimiento mejorado en reacciones catalíticas debido a sus sitios activos y la sinergia Pd-Ga.

Influenciando el futuro de la catálisis: esta tesis

El viaje de las nanoestructuras basadas en Pd para catálisis está lejos de terminar. Como investigadores, continuamos empujando los límites de lo que es posible en la nanoescala, explorando nuevas formas de optimizar propiedades y desarrollar asombrosas nanoarquitecturas.

Esta tesis revela los detalles intrincados de cómo estos nanocatalizadores basados en Pd fueron diseñados, fabricados y probados. Echemos un vistazo más de cerca al emocionante viaje que presenta.

Este trabajo comienza con la generación de nanopartículas de Pd mediante ablación por chispa y explora los efectos de varias configuraciones de cámara en la producción de nanopartículas a través de simulaciones y mediciones experimentales. Un paso adicional fue demostrar la producción de aleaciones Pd-Ga y la identificación de varias formaciones de fases con condiciones de operación variables. Posteriormente, un diseño innovador y fabricación de nanohilos semiconductores decorados con nanopartículas de Pd resultó en varios nanocatalizadores que fueron evaluados y probados para catálisis. Finalmente, avanzando las arquitecturas de nanocatalizadores mediante la fabricación de nanohilos de GaP ramificados, ¡creando estructuras tipo árbol a escala nanométrica!

Acknowledgements

Reflecting on this incredible journey, I am immensely grateful for the numerous individuals who have supported, guided, and inspired me throughout my doctoral studies.

First and foremost, I give thanks to Jesus, the Logos, God, and the Master Mind behind the universe's intelligent design, whose intricate laws and principles continue to inspire me in my scientific journey.

"Through him, all things were made…"- John 1:3

I extend my most profound appreciation to my supervisor, Maria. Your unwavering support, insightful guidance, and constant encouragement have shaped my research and my growth as a scientist. Thank you for believing in me and pushing me to reach my full potential.

I am equally grateful to my co-supervisors, Sara and Martin. Your diverse perspectives and expertise have greatly enriched my research knowledge. Martin, thank you for your guidance in COMSOL simulations and our numerous research discussions on approaching this novel work. Sara, thank you for introducing me to the fascinating catalysis world and allowing me to participate in beamtime projects at Max IV. Your combined mentorship has been essential in shaping my research journey.

To the entire Aerosol Group—Maria, Knut, Thomas, Linnéa, Pau, Mehran, Sam, Hajar, Mohammad, and former members Markus, Sara, and Calle—thank you for the group's collaborative spirit, intellectual discussions, and mutual support, which have created an environment where ideas flourish spontaneously. I cherish all the good memories, such as spending time with good food at Maria's and Knut's places, at work resolving the many intricate issues with the SDG and moving the SDG around like a large toy in the Physics department and at Max IV.

I want to express my sincere thanks to our collaborators at Kemicentrum. Daniel, your expertise and insights have been crucial in advancing our research. Leonard, your dedication and fresh perspectives have been both inspiring and helpful. Our collaborations have genuinely exemplified the power of interdisciplinary research.

For the paper on branched nanowires, I am deeply grateful to Crispin Hetherington for his exceptional work and for helping me learn more about TEM imaging on nanowires. Jonas Johansson, your modelling work has provided invaluable insights, bridging theory and experiments that have significantly enhanced my understanding of the nanowire field.

The nanocatalyst paper would not have been possible without the contributions of several key individuals. Sebastian, our thorough discussions across every detail of our paper, emphasising nanowire growth and TEM, have been enlightening and significantly improved our work's quality. Your passion for the field is contagious!

Namsoon, thank you for sharing your expertise on surface wettability and applying it to our nanowires. Nitul, your support in XPS characterisation and our numerous research discussions have helped shape the outcomes of this study. Once again, Daniel and Leo, your contributions to the catalysis section helped prove that our nanocatalysts work for catalysis!

I would be remiss if I didn't acknowledge the broader academic community at the Physics Division. To my friends and colleagues here, thank you for creating a supportive and stimulating environment. Our fika times, impromptu discussions, and shared experiences have made this journey intellectually rewarding and personally enriching.

My dearest friends Esther, Åsa, Asmita, Yue, and Kristi. Thank you for being there to enjoy good times and for supporting me through tough times.

Last but certainly not least, I want to express my sincere gratitude to my family. Your unconditional love, patience, and support have been my anchor throughout this challenging journey. You have celebrated my successes and supported me through the difficult times, often from a distance. Your belief in me has been a constant source of strength and motivation.

A special mention to my dad, now watching over me from heaven. Thank you for those words that constantly resonate in my mind and have become my life's motto and inner driving force:
"Nunca dejes de estudiar"
("Never stop learning").
I try to do that every day to honour your name and legacy. While I am still here, I will keep your spirit alive through my continuous pursuit of knowledge.

To everyone mentioned here and to those whose names I may have missed, your contributions, great and small, have played a crucial role in bringing this thesis to fruition. This work is as much a testament to your support and guidance as it is to my efforts. Thank you all for being part of this incredible journey.

List of Publications

I. Effects of Chamber Configurations on Nanoparticle Output in Spark Discharge Generators: A Combined CFD, Particle Tracing, and Experimental Study
M. Bermeo, D. Megyeri, M. H. Magnusson, A. Kohut, and M. E. Messing
In Manuscript

I performed the experimental and partly the COMSOL simulation work. I designed the chamber configurations and data analysis post-experimental and simulation studies. I wrote this paper with contributions from all authors.

II. Engineered Pd-Ga alloy nanoparticles through spark ablation and in-flight metal-organic precursor decomposition
M. Bermeo, M. Snellman, L. Jönsson, T. Krinke, Z. Li, K. Deppert, M.E. Messing
Manuscript submitted

I conceived the study together with coauthors. I carried out the experiments, characterised the samples, and analysed the data with support from the coauthors. I wrote this paper with contributions from all authors.

III. Semiconductor nanowire-supported palladium nanocatalysts: Design, fabrication, and surface characterisation
M. Bermeo, L. Schilling N. S. Rajput, S. Lehmann, N. Eom, S. Franzén, M. Tasić, M. H. Magnusson, D. Strand, and M.E. Messing
Manuscript submitted

I performed the nanocatalyst fabrication, starting from the optimisation of the nanowire growth recipes to the Pd nanoparticle deposition. I conducted microscopy characterisation and wettability analysis on the nanocatalysts. I wrote this paper with contributions from all authors.

IV. Branched-gallium phosphide nanowires seeded by palladium nanoparticles
M. Bermeo, S.M. Franzén, C. Hetherington, J. Johansson, M.E. Messing
Nanotechnology **2023**, 34, 395603

I developed the Pd-seeded nanowire and branch growth recipes, exploring the optimisation of the growth parameters. Likewise, I conducted the microscopy characterisation of the branched nanowires. I wrote this paper with contributions from all authors.

Papers not included in this thesis:

V. Enhanced LWIR response of InP/InAsP quantum discs-in-nanowire array photodetectors by photogate and ultra-thin ITO contacts

H. Jeddi, K. Adham, Y. Zhao, B. Witzigmann, F. Römer, M. Bermeo, M. T. Borgström, H. Pettersson

Nanotechnology **2024**, 35 (21), 215206

VI. Characterization and Toxic Potency of Airborne Particles Formed upon Waste from Electrical and Electronic Equipment Waste Recycling: A Case Study

I. Odnevall, M. Brookman-Amissah, F. Stábile, M. T. Ekvall, G. Herting, M. Bermeo Vargas, M. E. Messing, J. Sturve, L-A. Hansson, C. Isaxon, J. Rissler

ACS Environmental **2023**, Au 3 (6), 370-382

VII. Size-resolved characterization of particles> 10 nm emitted to air during metal recycling

K. Lovén, C. Isaxon, E. Ahlberg, M. Bermeo, M. E. Messing, M. Kåredal, M. Hedmer, J. Rissler

Environment International **2023**, 174, 107874.

VIII. Mo_3Ni_2N Nanoparticle Generation by Spark Discharge

J. E. Nordlander, M. Bermeo, P. Ternero, D. Wahlqvist, T. Schmeida, S. Blomberg, M. E. Messing, M. Ek, J-M. Hübner

Materials **2023**, 16 (3), 1113

IX. In Situ H_2 Reduction of Al_2O_3-Supported Ni- and Mo-Based Catalysts

S. M. Gericke, J. Rissler, M. Bermeo, H. Wallander, H. Karlsson, L. Kollberg, M. Scardamaglia, R. Temperton, S. Zhu, K. G. V. Sigfridsson Clauss, C. Hulteberg, A. Shavorskiy, L. R. Merte, M. E. Messing, J. Zetterberg, S. Blomberg

Catalysts **2022**, 12 (7), 755

Abbreviations

Au	gold
CFD	computational fluid dynamics
FWHM	full width at half maximum
Ga	gallium
H_2	hydrogen
MO	metal-organic
MOVPE	metalorganic vapour phase epitaxy
N_2	nitrogen
NP	nanoparticle
NW	nanowire
Pd	palladium
PH_3	phosphine
PT	particle tracing
SDG	spark discharge generator
SEM	scanning electron microscope
TEM	transmission electron microscope
TMGa	trimethyl gallium
STEM	scanning transmission electron microscope
EDX	Energy-dispersive X-ray spectroscopy
HAADF	High-angle annular dark-field imaging
SAED	Selected area electron diffraction
V/III	ratio between group V and III precursor partial pressures
VLS	vapour liquid solid
VSS	vapour solid solid
WZ	wurtzite
ZB	zincblende

1 Introduction

Nanotechnology has emerged as a transformative field in materials science and engineering, enabling the manipulation of matter at the nanoscale—dimensions ranging from 1 to 100 nm [1, 2]. This scale, approximately three orders of magnitude smaller than the diameter of a human hair, allows for the precise control of material properties and functionalities at the atomic and molecular levels. Nanomaterials exhibit unique physicochemical characteristics that differ significantly from their bulk counterparts due to quantum confinement effects and increased surface-to-volume ratios [1, 3]. These properties can be tailored by controlling nanostructure size, shape, composition, and morphology, leading to novel applications across various disciplines.

One of the most promising areas of nanotechnology research is the development of nanocatalysts. These nanoscale catalytic systems offer enhanced reactivity, selectivity, and efficiency compared to traditional catalysts due to their high surface area and unique electronic structures [1] . Nanocatalysts have found applications in diverse fields, including medicine, food industry, and sustainable energy technologies.

1.1 Nanocatalysts

In 1835, the Swedish chemist Jöns Jacob Berzelius (1779-1848) coined the term "catalysis" and stated that "*catalysis is more common than believed, part of inorganic and organic nature*"[4]. Later in 1894, Ostwald defined catalysis as *"the acceleration of a chemical reaction which proceeds slowly, through the presence of a foreign substance"*[5]. Indeed, a catalyst accelerates a reaction by lowering its activation energy. Nowadays, catalysis is involved at some point in the processing of over 80% of all manufactured products [6], and nanocatalysts are gaining terrain in this field.

Nanocatalysts, consisting of nanoparticles with dimensions of 1-100 nm, combine the advantages of homogeneous and heterogeneous catalysis (Figure 1.1). Their high surface area-to-volume ratio, increased reactivity, and enhanced mass transport often result in unique catalytic properties compared to bulk materials [3]. Nanocatalysts based on nanoparticles belong to the class of heterogeneous catalytic systems, also known as solid-state catalysts, where the catalyst is present in a different phase from the reactants or products.

These heterogeneous nanocatalysts can be produced via top-down and bottom-up approaches. Top-down methods involve the mechanical or chemical fragmentation of bulk materials, while bottom-up methods control nucleation and growth of nanoparticles from small molecular precursors. Bottom-up approaches are often preferred since they offer better control over nanoparticle size, shape, and composition. Nanocatalysts face challenges in long-term stability and durability under harsh reaction conditions. The high surface area and reactivity of nanoparticles make them susceptible to sintering, oxidation, and poisoning, leading to a decrease in catalytic activity over time [7]. Strategies such as stabilising agents, doping, and incorporating NPs onto high surface area supports have addressed these issues.

The support plays a crucial role in maintaining NP stability, catalytic performance, and facilitating separation for reuse. Proper selection of support materials is essential, based on specific application requirements and catalytic system needs.

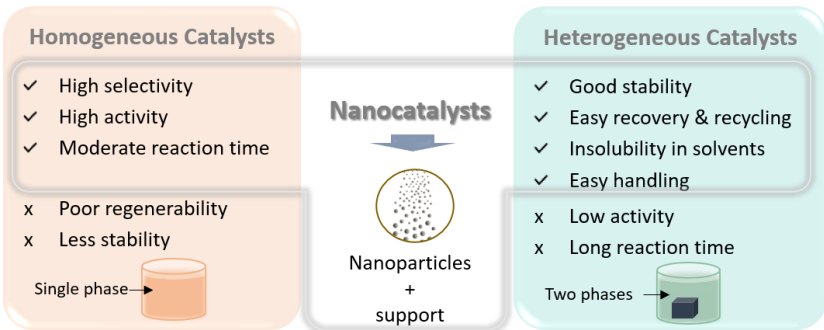

Figure 1.1. Advantages and disadvantages of homogeneous catalysts, heterogeneous catalysts, and nanocatalysts.

1.2 Pd-based Nanostructures for Catalysis

The development of nanostructures begins with careful material selection and composition, all the way to their properties, morphologies, and functionalities. A particularly intriguing area of research addressed in this thesis involved the fabrication of palladium (Pd) based nanocatalysts.

Pd nanoparticles and GaP nanowires

Pd nanoparticles are well-known for their excellent catalytic properties, especially in hydrogenation reactions [8] and C-C coupling reactions [9], among the most valuable organic transformations and synthesis reactions. Pd is a transition metal with a ground-state electron configuration [Kr] $4d^{10}$ $5s^{0}$, giving it a d^{8} configuration in its common +2 oxidation state. This results in a square-planar geometry with two open axial coordination sites, which allows reactants like alkenes or hydrogen to bind effectively, making it a suitable catalyst.

Combining Pd nanoparticles with appropriate supports can enhance their stability and catalytic properties, facilitating their separation for reuse and minimising the loss of nanoparticles. Gallium phosphide (GaP) in the form of nanowires is a semiconductor that has recently been studied for various applications such as catalysis, hydrogen storage, and biomedicine [10-15]. Due to their high aspect ratio (length to diameter), GaP nanowires can serve as supports for Pd nanoparticles, providing a larger surface area, thereby increasing the exposure of the nanoparticles. In addition, the biocompatibility of GaP nanowires widens the range of applications and makes them attractive for exploring potential synergy effects. Thus, this innovative approach of supporting Pd nanoparticles on nanostructured materials like GaP nanowires offers great potential for enhancing catalytic performance.

The fabrication process of these Pd-based nanocatalysts combines state-of-the-art techniques, such as spark ablation for nanoparticle generation and metal-organic vapour phase epitaxy (MOVPE).

Multielement aerosol compounds

The nanoparticle tuneability of spark ablation is extended not only to the generation of pure metals but also oxides (e.g., CdO, Fe_2O_3, MgO)[16, 17], non-alloyed composites (e.g., Ag-C, Mg-Pt, Mg-Nb)[18, 19], alloys (e.g., Ag-Au, Cu-Ni, Pd-Cu, Cr-Co, Au-Pd, Ag-Pd) [20-24], and even nanoalloys of immiscible bulk metals (e.g., Au-Pt, Ag-Cu, Cu-W) [25]. When exploring Pd-based alloys for catalysis, Pd-Ga alloys offer potential synergetic effects and multiple catalytic applications. Recent studies have shown that Pd-Ga intermetallic compounds, such as PdGa and Pd_3Ga_7, demonstrate high selectivity in hydrogenation reactions [26, 27].

Hybrid approach: Branches and Pd-Ga phases

The combination of spark ablation and MOVPE allows the development of more complex nanostructures such as nanotrees. Pd nanoparticles deposited on GaP nanowires can be used as seeds to grow branches (Figure 1.2), thus increasing the surface area and potentially developing Pd-Ga phases attractive for catalysis.

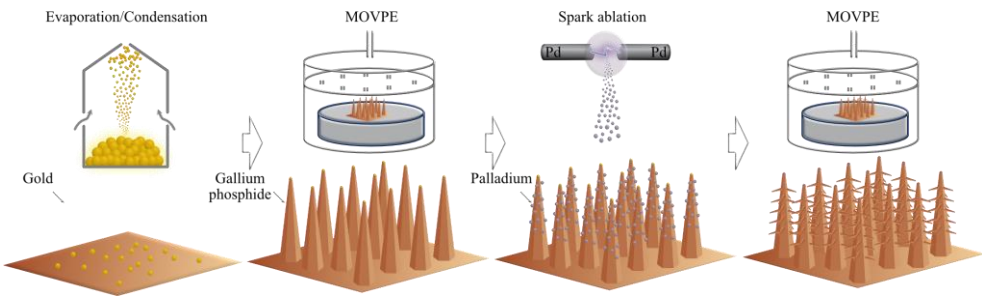

Figure 1.2. Schematic representation of the fabrication process of Pd-based nanostructures for catalysis from Au nanoparticle generation via evaporation/condensation methods, followed by nanowire growth through MOVPE, Pd nanoparticle generation and deposition using spark ablation, and finally, branch growth using MOVPE.

1.3 Scope

This thesis explores the design, synthesis, and application of advanced nanostructures as potential nanocatalysts leveraging palladium nanoparticles and innovative support structures, including gallium phosphide nanowires and Pd-Ga alloys. The following chapters are structured as follows:

Chapter 2 introduces the aerosol methods for generating engineered nanoparticles: evaporation/condensation and spark ablation. Additionally, an evaluation of the effect of several chamber configurations on nanoparticle output via simulations complemented by experimental measurements is presented (**Paper I**). Also, the exploration of Pd-Ga alloy nanoparticles is shown by combining a dual-process approach with spark ablation and injecting a metal-organic precursor (**Paper II**).

Chapter 3 presents the physics of nanowire growth and branch growth through MOVPE. The effect of growth parameters, including temperature and V/III ratio, to control the nanowires' resulting morphology and crystal structure is discussed (**Papers III & IV**).

Chapter 4 lists all the nanocatalysts, detailing the fabrication steps and techniques for nanoparticle generation and nanowire support.

Chapter 5 describes the theory of wettability in different regimes. This supports the experimental work on surface wettability analysis performed on the candidate nanocatalysts for subsequent catalytic tests.

Chapter 6 analyses the catalytic performance of the candidate nanocatalysts, including Pd-Ga nanoparticles and semiconductor nanowire-supported palladium nanocatalysts, and the observed parameters affecting their catalytic activity. This chapter is based on the nanocatalysts developed in **Papers II & III**.

Chapter 7 summarises the work done in this thesis, providing an outlook on the future of these nanostructures as potential catalysts.

2 Engineered Catalytic Nanoparticles

Aerosol-based techniques present numerous advantages for particle generation over conventional wet-chemical synthesis methods. For example, it is possible to obtain high-purity nanoparticles due to the absence of chemical reagents, to tune particle morphology producing core-shell and Janus structures [28, 29], and to form new alloys and compounds from immiscible bulk metals owing to the fast cooling of the particle stream [30, 31]. Some of the typical aerosol-based techniques include evaporation/condensation, plasma synthesis, spark discharge generators, and flame spray pyrolysis, among others [32-34].

This section focuses on evaporation/condensation and spark ablation methods, which are central to this thesis. These approaches offer precise control over particle morphology, size, composition, and concentration and were used as building blocks for fabricating nanostructures for catalysis.

2.1 Evaporation/Condensation

The evaporation/condensation aerosol method, as depicted in Figure 2.1, is described by Magnusson et al. [35]. A desired material (e.g., Au) in the form of small pellets is placed in a crucible inside the hot zone of a high-temperature furnace, which is heated to temperatures above 1500 °C, where material evaporation occurs. A carrier gas (e.g. N_2) transfers the evaporated material out of the heating compartment and exits the furnace. The rapid cooling and low vapour pressure of the metal at nearly room temperature (Au: $\sim 10^{-23}$ Pa) allows the supersaturated vapour to readily nucleate, forming atomic clusters, which then condense into fine nanoparticles and finally form agglomerates [36].

Using a sintering furnace and differential mobility analyser (DMA), as explained in section 2.2, the as-produced agglomerates can be compacted and size selected, producing spherical, -monodisperse nanoparticles [37-39].

These nanoparticles can be used for different purposes, such as catalytic seeding particles for nanowire growth, as described in **Chapter 3**.

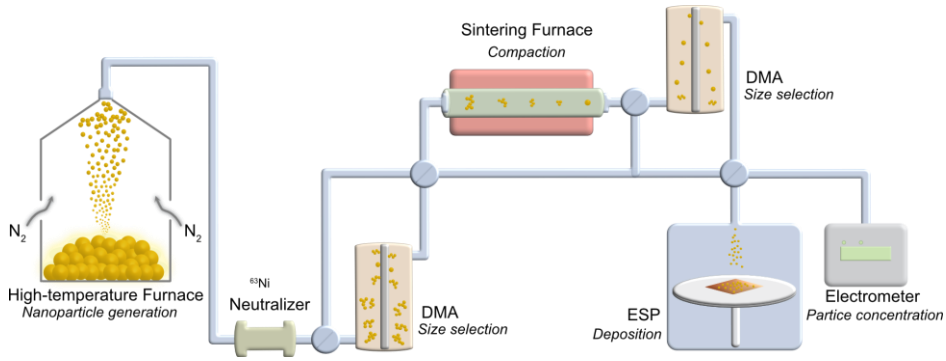

Figure 2.1. Schematic of an aerosol system through evaporation/condensation using a high-temperature furnace, size selection, and a sintering furnace.

2.2 Spark Ablation

A spark ablation system or a spark discharge generator (SDG) [40, 41] comprises two adjustable electrodes positioned a few millimetres apart. The RLC (resistance, capacitance, inductance) electric circuit of the SDG includes a high-voltage power supply that charges a capacitor (19 nF), providing the necessary energy to generate a spark plasma at the electrode gap (Figure 2.2). The capacitor cyclically discharges, producing sparks at a frequency determined by the current (I) charging the capacitor, capacitance (C), and discharge voltage (V_d) as described by Eq. 2.1 [42, 43]. Each spark locally ablates material from the electrode surfaces, leading to evaporation and subsequent nanoparticle generation, as described below.

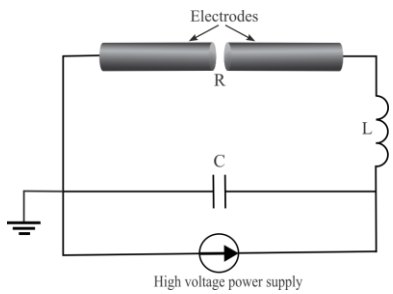

Figure 2.2. Schematic of the equivalent RLC electric system of spark ablation.

$$f = \frac{I}{CV_d} \qquad \textit{Eq. 2.1}$$

Formation mechanism of nanoparticles

Each spark between the electrodes generates a high-temperature plasma ranging from thousands to tens of thousands of Kelvin [44, 45] that lasts a few microseconds, causing

instant, localised electrode surface heating. Upon spark extinction, a vapour plume of ablated material is formed in the electrode gap. This high-energy vapour undergoes rapid cooling through adiabatic expansion and mixing with the surrounding carrier gas, leading to a high supersaturation. Through intensive particle-particle collisions, small atomic clusters form, nucleate, and grow by complete coalescence into primary particles with a size of a few nanometres [46]. Continuous particle growth occurs when these primary particles collide with one another, reducing their surface energy and resulting in the formation of either new spherical particles (i.e., complete coalescence) or agglomerates (i.e., partial coalescence, when the collision rate is faster than the coalescence rate) [47]. The carrier gas transports the generated particles away from the heated zone. Figure 2.3 illustrates the process from the spark to particle formation. Depending on the electrode composition, various aerosol particles can be produced, including pure metals, non-alloyed composites, alloys, semiconductors, oxides, hydrides, etc. [48].

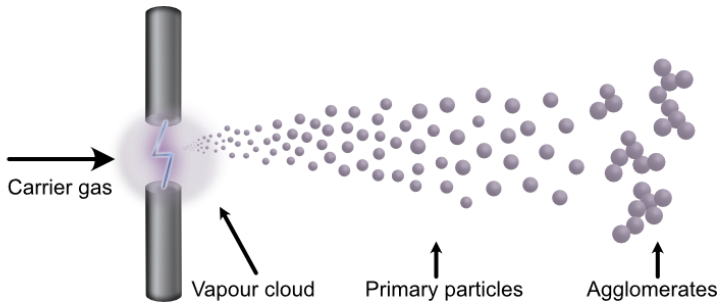

Figure 2.3. Schematic representation of the particle formation near the electrode gap through nucleation and collision-coalescence process.

Compaction, size selection, and deposition

Figure 2.4 illustrates a schematic representation of an SDG setup designed for the generation, reshaping, size selection, and deposition of nanoparticles onto a support [34]. The electrodes are typically arranged in a rod-to-rod configuration (i.e., parallel cross-sections) housed within an airtight chamber. A continuous flow of a carrier gas (e.g., N_2) is introduced at atmospheric pressure and ambient temperature to facilitate the transport of ablated material throughout the system.

The particle generation process is initiated within the chamber by spark discharges. The gas flow transports the resulting fractal-like agglomerates to a neutralizer, acquiring a *Boltzmann equilibrium* charge distribution, also called steady-state or bipolar equilibrium charge distribution [49]. Subsequently, a DMA is employed to perform an initial size selection based on the electrical mobility of the particles [49]. The electrical mobility diameter is equal to the geometrical diameter for spherical particles. Downstream of the first DMA, the sintering furnace operating at high temperatures (material dependent) promotes the compaction and sintering of agglomerates into quasi-spherical nanoparticles. A second DMA further refines the size selection, producing monodispersed nanoparticles with diameters ranging from ca. 10 to 100 nm [50].

Finally, the particles are deposited onto wafer substrates within an electrostatic precipitator (ESP). The deposition spot radius in the ESP was found to be dependent on the carrier gas flow rate (Q), the distance between the inlet and deposition platform of the ESP (h), the ESP potential (φ), and the electrical mobility of the nanoparticles (Z) as described by the semi-empirical Eq. 2.2, developed by Preger et al. [51]:

$$r_{spot} = \kappa \sqrt{\frac{Q.h}{\varphi.Z}} \qquad \textit{Eq. 2.2}$$

Here κ is a dimensionless constant. Additionally, the deposition time (t) required to achieve a desired spot concentration (c_{spot}) at an average particle gas concentration (c_{gas}) can be calculated using Eq. 2.3:

$$t = \frac{\pi.r_{spot}^2.c_{spot}}{Q.c_{gas}} \qquad \textit{Eq. 2.3}$$

Moreover, by diverting the nanoparticle stream to an electrometer instead of the ESP, the c_{gas}, also called particle number concentration, can be quantified, as the induced current measured by the Faraday cup of the electrometer is proportional to the number of charged particles.

As a separate remark, the evaporation/condensation method described above includes the devices explained in this section for size selection, particle sintering, and deposition.

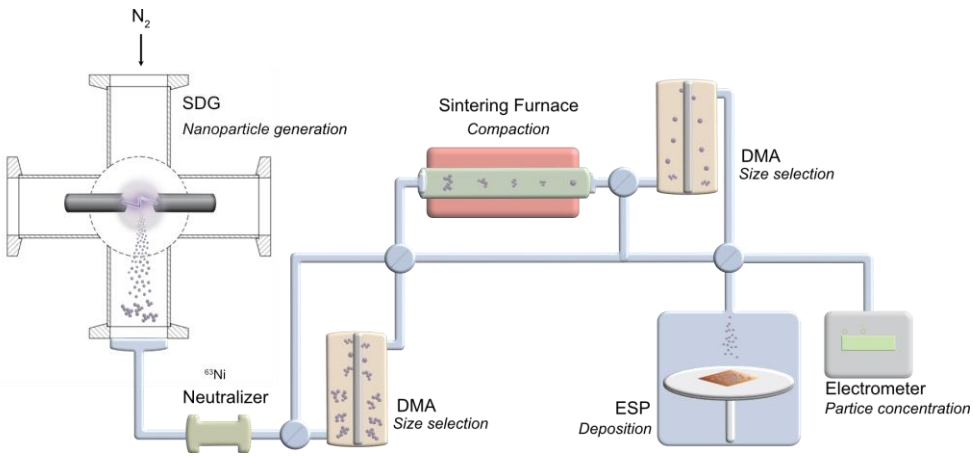

Figure 2.4. Schematic of a spark ablation system. Nanoparticles are generated by spark ablation, forming agglomerates. The agglomerates get a known charge distribution when they pass through a neutralizer and are size selected in a differential mobility analyser (DMA). Afterwards, particles are compacted in a sintering furnace, and they can be size selected again to finally be deposited using an electrostatic precipitator

2.3 Palladium Nanoparticles

Pd is a well-known catalyst widely used in C-C coupling reactions [52] and hydrogenation and dehydrogenation reactions [53] which are essential in organic synthesis for the formation of complex molecules and the selective addition or removal of hydrogen from organic compounds, respectively.

This research used Pd nanoparticles as building blocks for nanocatalyst fabrication and branched nanowire growth, as described in **Paper III** and **Paper IV**, respectively, and further discussed in **Chapters 3** and **4**. Therefore, the first step included generating high-purity Pd nanoparticles of defined morphology. Pd rod electrodes with a diameter of ca. 3.00 mm were employed as the anode and cathode in the SDG setup described earlier. The agglomerated Pd nanoparticles produced by the SDG are predominantly polycrystalline and comprise primary particles.

The particle size distribution of Pd nanoparticles generated in the SDG typically ranges from 1 nm to 100 nm in a log-normal distribution with a variable peak mobility diameter (~30 nm in Figure 2.5a) depending on the operating conditions such as electrode gap, discharge voltage, and current.

The agglomerated Pd nanoparticles formed in the SDG undergo thermal sintering at 750 °C to achieve spherical morphology. This sintering temperature is appropriate for the compaction of Pd nanoparticles since the mobility diameter remains relatively constant at higher temperatures, indicating that the particles have reached a fully compacted state [41]. The Pd nanoparticles usually show a spherical shape with predominantly single crystalline structures (Figure 2.5 b and c).

When using a DMA (upstream and/or downstream of the sintering furnace) at a selected particle size, it is possible to obtain monodisperse Pd nanoparticles (10 nm diameter of Pd nanoparticles in Figure 2.5b).

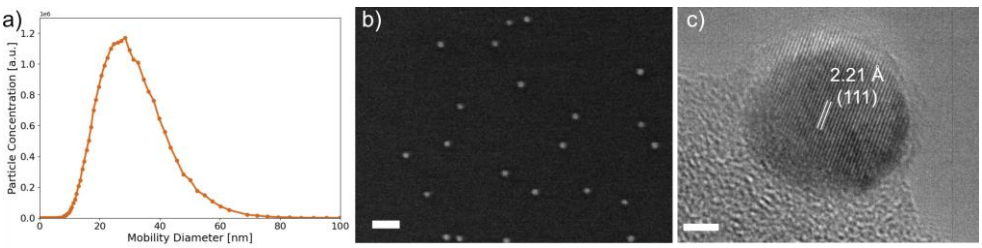

Figure 2.5. a) Particle size distribution of Pd nanoparticles using a DMA downstream the sintering furnace, obtained at 2 mm electrode gap and 10 mA; b) SEM and c) HRTEM of 10 nm Pd nanoparticles. Scale bar b) 50 nm, c) 2nm.

2.4 Particle Output Dependence on Chamber Configurations

The versatility of spark ablation has an increasing potential for industrial-scale nanoparticle production. The ability to upscale nanoparticle synthesis methods is essential for future commercialisation in catalysis. Spark ablation offers a promising pathway, provided its particle generation rates can significantly improve. Alongside extensive research on optimising operating conditions of the SDG [41, 54], a fundamental approach involves investigating chamber configuration parameters, such as chamber volume, electrode placement, and inlet/outlet positioning, as described in **Paper I** and presented in this section.

Chamber configurations

The efficiency of nanoparticle generation and transport in an SDG is intrinsically tied to the chamber's flow dynamics. The complex relationship between chamber design and particle behaviour was investigated through Computational Fluid Dynamics (CFD) and Particle Tracing (PT) simulations and complemented with experimental measurements to validate these computational models. The simulations were conducted using COMSOL Multiphysics® software (COMSOL, Inc.). Previous studies have used CFD to model the effect of flow geometries on particle output [55] and variations in electrode configurations [56] providing insights into the critical parameters for modelling in spark ablation.

An SDG, as described in section 2.2, was used in several chamber configurations. The existing chamber (E) (Figure 2.6 a) with inner inlet and outlet tubes at 47.2 mm from the electrode surface was adapted by adding longer inner and outlets (at 10 mm from the electrode surface), as well as from 2 to 6-airtight blocks on the sides of the chamber, named from 0B to 6B, according to the number of blocks (Figure 2.6 b), thus reducing their inner chamber volume from 400 to 75 cm^3.

Laminar flow simulations

CFD simulations show the flow velocity of the carrier gas with a zoom-in near the electrodes (Figure 2.6 b). The velocity profiles of the carrier gas were analysed along the chamber axis from the inlet to the outlet of every SDG chamber, with the electrode gap positioned at the centre (x = 0 in Figure 2.6 c). The results showed that all modified chamber configurations exhibited nearly identical velocity profiles, primarily due to the proximity of the inlet and outlet tubes to the electrodes. In contrast, chamber E displayed the lowest overall velocity profile due to its longer flow paths and higher flow recirculation. The difference in peak velocity at the electrode gap significantly increased from ~0.8 m/s in chamber E to 2.6 m/s in the modified chamber configurations. A higher velocity favours dilution and reduces particle collision-coalescence, resulting in higher concentrations of smaller particle diameters [57].

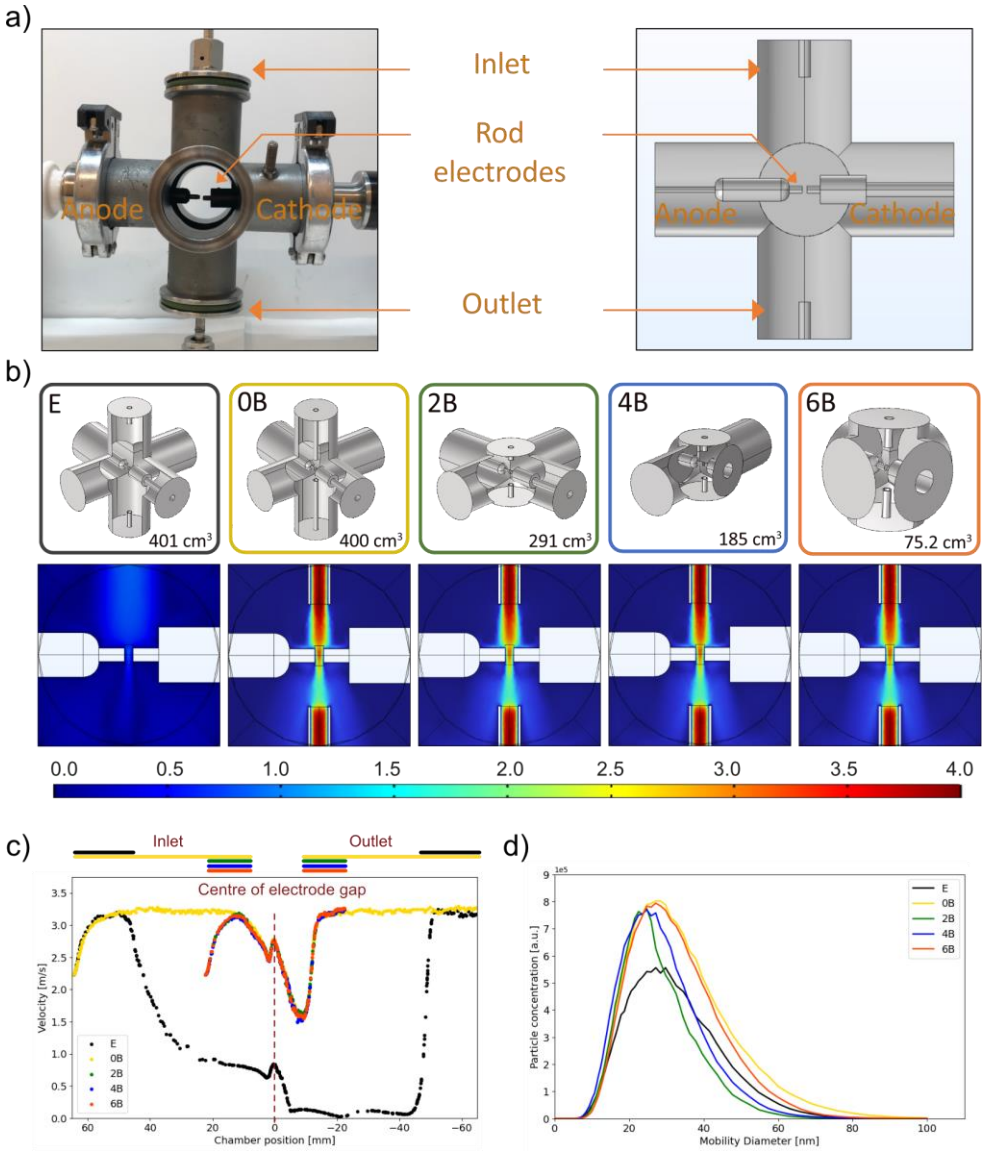

Figure 2.6. a) Front view of spark discharge generator(SDG) of an existing chamber (E) configuration (left) and its corresponding model geometry from Comsol (right), b) SDG of several chamber configurations and their corresponding velocity profiles after Computational Fluid Dynamic (CFD) simulations and c) CFD in laminar flows from the edges of the inlet to the outlet and d) experimental particle size distributions for several SDG chamber configuration measured at 2 mm electrode gap, 10 mA and 10 kV driving current and voltage, respectively.

Experimental particle output

Preliminary experimental measurements were validated at the same 2 mm electrode gap, using a DMA downstream of the sintering furnace and an electrometer to measure

the particle output. The findings showed a higher particle concentration for modified configurations than chamber E. The comparable particle output among the modified configurations indicates that changes in inlet/outlet positioning, placing them closer to the surface electrodes, have a more predominant impact than the chamber volume reduction. It is worth noting that variations in particle concentration across the modified configuration may be influenced by several factors, such as the precision of placing the rod electrodes with parallel cross-sections at the specific electrode gap and the fluctuations in discharge voltage and spark frequency, among others.

Particle tracing simulations

Particle Tracing (PT) simulations are a natural continuation of flow simulations, and their outcome depend on selecting appropriate input parameters that reflect realistic operating conditions, including carrier gas flow dynamics, mesh size geometry, and nanoparticle properties (e.g., size distribution and electrical mobility). For this evaluation, a predefined cylindrical volume of 31.8 mm^3 was located at the electrode gap to simulate particle release from the electrodes.

Preliminary PT results (Figure 2.7) showed that the modified chamber configuration exhibited the highest transmission probability, ranging from 90.7% to 94.4% out of 100,000 virtual particles, as well as the shortest residence time between 35.2 ms and 36.6 ms at 90% of the particles that reach the outlet. On the contrary, configuration E showed a lower transmission probability of 25.7% and a longer residence time of 397.7 ms. These differences are related to the flow paths that vary particle recirculation inside the chamber. The modified configuration showed a straight particle trajectory towards the outlet, whereas configuration E shows deviations in particle trajectory due to a longer flow path (Figures 2.7 b and c).

These PT results indicate that the modified chamber configurations (0B, 2B, 4B, and 6B) showed comparable performance, superior to configuration E, which are coherent with CFD and experimental findings, and suggesting that shorter distances from the electrode to the inlet/outlet have a more significant impact on particle output.

Additional studies are essential to model various SDG chambers, including the effects of electric fields at the electrode gap, charged particles, and other particle generator geometries.

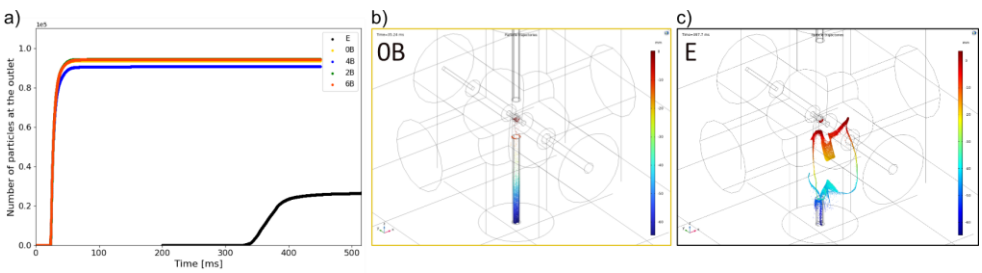

Figure 2.7. Particle tracing simulations. a) Number of particles at the outlet of various SDG configurations. Particle trajectories for b) configuration 0B and c) configuration E.

Impact of particle output on nanocatalyst fabrication

The effect of chamber configuration on particle output was experimentally tested during nanocatalyst fabrication. During nanoparticle generation and using Eq. 2.2 and Eq. 2.3, it was possible to estimate the deposition spot radius (r_{spot}), which must be sufficient to cover the entire nanocatalyst area at a reasonable deposition time (t).

Our SDG setup's experimental values for Q, h, φ, and Z are 1.68 lpm, 12 mm, 2 kV, and 2.14×10^{-6} (for 10 nm particle size), respectively. Using these parameters, during the nanocatalyst fabrication (C**hapter 4**), 10 nm Pd nanoparticles were deposited along nanowire supports in a c_{spot} of 1000 μm^{-2} over an 8 mm x 8 mm wafer. With the existing chamber (E) at a measured c_{gas} of $10^5 \pm 10^3$ cm^{-3}, this process required an average deposition time of 7.8 ± 0.8 hours.

A significant improvement in deposition efficiency was achieved by switching to a modified chamber configuration. For instance, using chamber 0B, the measured average c_{gas} increased to $1.54 \times 10^5 \pm 6 \times 10^3$ cm^{-3}, which reduced the average deposition time to 5.1 ± 0.2 hours while maintaining the same nanoparticle concentration, representing a 34.6 ± 8.3 % reduction in deposition time. This substantial enhancement in nanoparticle output highlights the importance of further optimising the SDG to increase the particle output and reduce the deposition time for its adoption in commercial-scale applications.

2.5 Pd-Ga Alloy Nanoparticles

Generating alloy nanoparticles with low-melting-point materials challenges traditional spark ablation due to potential electrode melting under high-energy conditions of the spark. To address this limitation, an alternative approach consists of using a precursor of the low melting point material, such as a hydride [58] or a metal-organic [59], which then alloys with the aerosol nanoparticles.

Pd-Ga synergy

The importance of Pd-based nanomaterials for catalysis has led to investigations of alloying Pd with other elements to enhance catalytic performance, durability, and cost-effectiveness.

The synergistic effects of Pd-Ga are attractive in catalysis. The presence of Ga in intermetallic Pd-Ga compounds are desirable to suppress the formation of reactive hydrides phases [60]. Also, Pd-Ga are candidates for various catalytic applications. For instance, in CO_2 hydrogenation, Pd_2Ga and Pd_5Ga_2 catalysts demonstrate high activity and selectivity towards methanol production [61-63]. For acetylene hydrogenation, PdGa, Pd_2Ga, and Pd_3Ga_7 exhibit good selectivity for ethylene formation, effectively suppressing the over-hydrogenation to ethane [60, 64, 65].

Tuneable Pd-Ga intermetallic compounds

The generation of Pd-Ga compounds through spark ablation presents unique challenges due to the low melting point of Ga, making its use as an electrode impractical. Thus, a Ga precursor such as trimethyl gallium (TMGa) {$Ga(CH_3)_3$}, stored in a bubbler at -10 °C, was a suitable alternative. TMGa readily decomposes in the sintering furnace at temperatures above 550-660 °C in N_2 [66, 67] removing methyl (CH_3) organic ligands and releasing Ga atoms that alloy with Pd nanoparticles produced in the SDG (Figure 2.8).

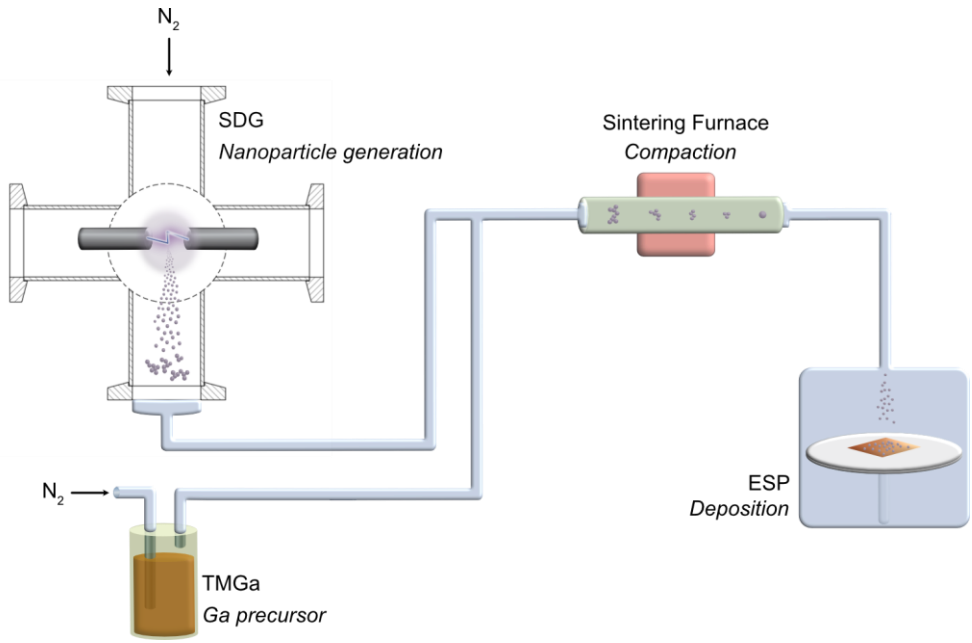

Figure 2.8. Setup of SDG and TMGa injected downstream the SDG and upstream the sintering furnace to produce Pd-Ga alloy nanoparticles.

The synthesis of Pd-Ga alloy nanoparticles was investigated using TMGa flow rates set at 1, 3, and 5 sccm, corresponding to TMGa molar fractions of approximately 3.7 x 10^{-5}, 11.2 x 10^{-5}, and 18.6x10^{-5}, respectively, and sintering temperatures of 750°C and 900°). The study revealed the significant influence of these parameters on the morphology, composition, and phase formation of the resulting nanoparticles. The effect of the sintering temperature in the particle morphology is evident at high TMGa flow rates, resulting in increasing particle size at 900 °C, likely due to a higher number of available Ga atoms from a more efficient TMGa decomposition. According to STEM-EDX compositional analysis, significant differences were observed at low TMGa flow rates (1 sccm) for particles smaller than 10 nm in diameter (Table 2-1). At 750 °C, Pd-rich phases (96.6 ± 3,4 at.% Pd) suggest limited Ga diffusion in the particles, likely due to the increased vapour pressure of Ga within small-diameter

particles. In contrast, at 900 °C, Pd-rich phases with 75.8 ±8.47 at% Pd formed. The increase in Ga content likely results from a combination of higher Ga vapour pressure within the particles (leading to Ga loss)and greater availability of Ga atoms diffusing into the particles.

Table 2-1. Pd-Ga particle composition for a TMGa flow of 1sccm at 750 °C and 900 °C, for particles ≤ 10 nm diameter.

Sintering temperature [°C]	Pd [at%]	Ga [at%]	Std. Deviation [at%]
750	96.61	3.39	3.22
900	75.83	24.17	8.47

The effect of increasing TMGa concentrations showed significant morphology variation in particles at 900 °C, resulting in particle growth, Pd aggregation, and the formation of tail-like structures with amorphous Ga-rich phases (Figure 2.9). At TMGa of 1sccm, nanoparticles exhibit a uniform distribution of Pd and Ga, suggesting a stable alloying process. At the TMGa of 3 sccm and 5 sccm, there is enhanced Ga incorporation and potential surface segregation with clear Ga-rich dominated phases. At this temperature, several phases were identified through HASDF-STEM imaging and EDX mapping along with HRTEM: Pd_5Ga_2(at 1 sccm of TMGa), Pd_5Ga_2 and Pd_2Ga (at 3 sccm of TMGa), and PdGa (at 5 sccm of TMGa). As mentioned above, all these Pd-Ga phases have been investigated for their catalytic properties.

These results demonstrate that integrating spark ablation with metal-organic precursor decomposition offers a versatile approach for synthesising Pd-Ga alloy nanoparticles with tailored compositions. Further investigations focusing on optimising precursor supply and sintering time could enhance control over the Pd-Ga phase compositions.

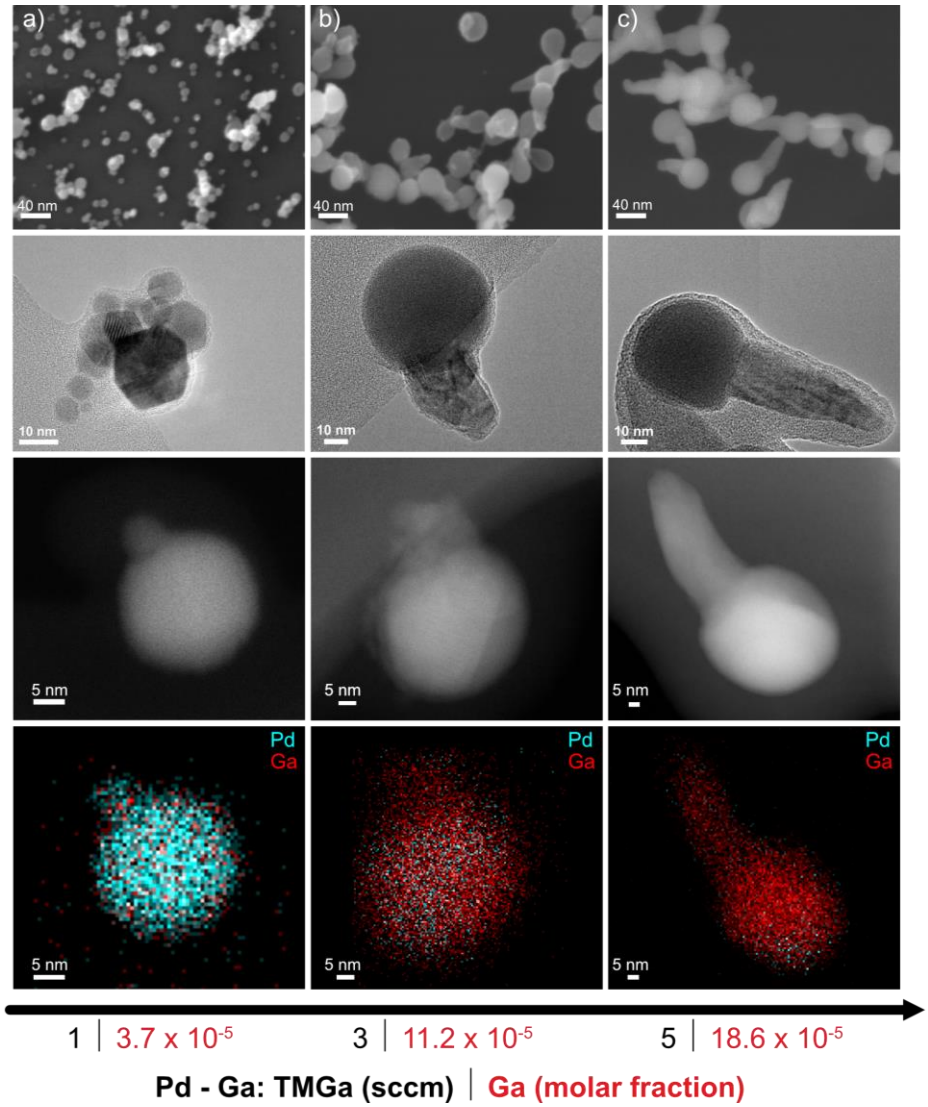

Figure 2.9. SEM (1st row), TEM (2nd row), STEM (3rd row), and EDX (4th row) micrographs of Pd-Ga alloy nanoparticles produced at 900 °C at a) TMGa = 1 sccm, b) TMGa = 3 sccm, and c) TMGa = 5 sccm.

3 Semiconductor Nanowire Supports

Several studies have explored the use of semiconductors as supports to enhance the catalytic activity of Pd catalysts [68, 69]. Standing semiconductor nanowires offer a novel pedestalled support design with distinct advantages. These 1D materials, with high aspect ratios and diameters ranging from 5-200 nm [70], provide large surface areas for improved nanoparticle distribution and reduced aggregation.

Semiconductor nanowires are typically grown using bottom-up approaches, wherein atomic layers are sequentially deposited on a substrate of the same or different semiconductor material. A widely applied technique for nanowire growth is metal-organic vapour phase epitaxy (MOVPE), which is essential in fabricating nanowire supports with specific features for the nanocatalysts presented in this thesis.

To provide context for the main findings of **Papers III** and **Paper IV**, which discuss nanowires seeded by Au and Pd nanoparticles, respectively, it is essential to introduce the fundamental concepts of MOVPE and nanowire growth mechanisms.

3.1 Metal-Organic Vapour Phase Epitaxy

MOVPE, also referred to as metal-organic chemical vapour deposition (MOCVD), consists of two parts identified as the gas delivery and reactor (Figures 3.1 and 3.2). MOVPE involves transporting constituent elements in the gas phase via a carrier gas, typically at ~100 mbar. The gaseous precursors undergo thermal dissociation, releasing atoms at the vapour-solid interface where layer growth occurs.

In the nanowire growth process, metal-organic (MO) and hydride precursors are introduced into a reactor along with a carrier gas (H_2). For GaP nanowire growth, trimethylgallium (TMGa) and phosphine (PH_3) serve as group-III and group-V precursors, respectively. TMGa is stored in the liquid phase in a bubbler. The carrier gas becomes saturated with TMGa molecules upon introduction into the bubbler. PH_3, characterised by its high vapour pressure, is stored in a pressure bottle at ~500 psi and at room temperature. Precise control of precursor flow rates is achieved using mass flow controllers (MFCs). The (111) B GaP wafer piece containing catalytic seed

particles (e.g., Au or Pd) is loaded into the reactor, which is heated, and the precursors are injected where the nanowire growth occurs.

In this work, two distinct MOVPE systems were employed. For **Paper III**, a vertical closed coupled showerhead reactor MOVPE (Aixtron CCS) was used (Figure 3.1), where the precursor injection is perpendicular to the wafer.

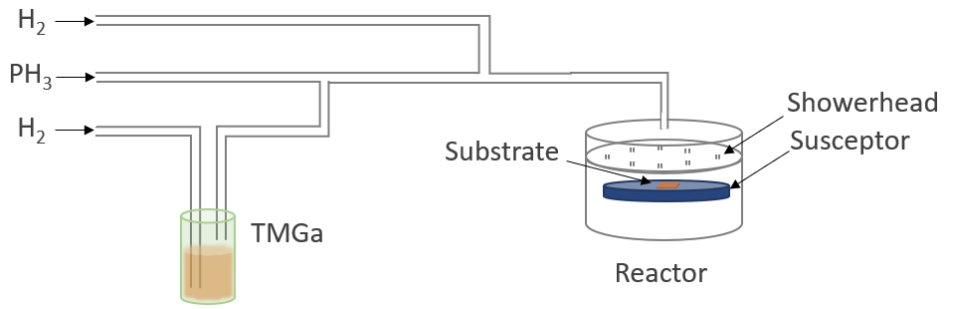

Figure 3.1. Schematic diagram of a vertical closed coupled showerhead reactor MOVPE (Aixtron CCS) setup used in both Au-seeded and Pd-seeded GaP nanowire growth. Three main lines are shown: hydrogen, phosphine, and TMGa as group V and III precursors, respectively.

Paper IV used a horizontal quartz reactor MOVPE (Epiquip VP502-RP). This system is equipped with a graphite susceptor aligned with a quartz tube inserted into the reactor, where precursors are injected parallel to the wafer (Figure 3.2).

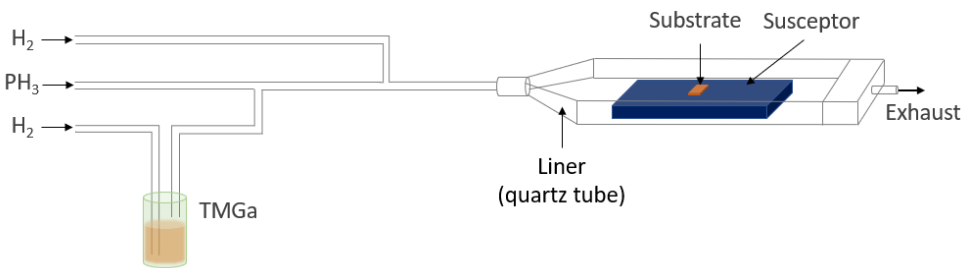

Figure 3.2. Schematic diagram of MOVPE Epiquip setup used to fabricate Pd-seeded GaP nanowires. Three main lines are shown: hydrogen, phosphine and TMGa as group V and III precursors, respectively.

3.2 Nanowire Growth Mechanisms

Vapor-liquid-solid (VLS) and vapor-solid-solid (VSS) are the primary semiconductor nanowire growth mechanisms models. In these models, the vapour is referred to as the state of the precursor gases; either liquid or solid refers to the physical state of the catalytic particle during nanowire growth, whereas solid is the nanowire crystal.

In the VLS mechanism growth model (Figure 3.3), nanowire growth occurs from a liquid metal catalyst droplet acting as a seed particle. The metal catalyst is heated, then melts and reacts with the precursor gases, primarily forming an alloy with the group III precursor. As precursor gases are supplied, they diffuse into the liquid droplet, leading to supersaturation, resulting in the nucleation of the group III and V elements, forming the nanowire crystal [71, 72]. The nanowire then grows through a steady-state process, incorporating atoms from the liquid droplet at the seed particle-nanowire interface [73]. Growth via the VLS mechanism is generally preferred since it promotes high axial growth rates [74, 75], stable growth direction [72], and crystal phase control [76]. This mechanism is observed in GaP nanowires seeded by Au nanoparticles, as described in **Paper III**, and in straight GaP nanowires seeded by Pd nanoparticles, as described in **Paper IV.**

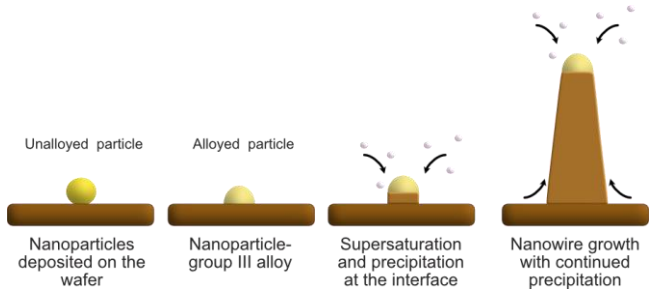

Figure 3.1. Vapour liquid solid growth (VLS) mechanism of III-V semiconductor nanowires.

Conversely, the VSS growth mechanism involves nanowire growth from partially or completely solid seed particles. In this process, precursor gases primarily adsorb onto and diffuse along the surface of the seed particle. The precursor gases react and decompose, leaving the group III and V atoms to diffuse along/through the seed particle-nanowire interface, where nucleation and growth occur, while the seed particle remains predominantly solid throughout the process [77, 78]. The VSS growth mechanism often results in lower growth rates [79] and unstable growth directions [80]. Paper IV describes that VSS is observed in mostly kinked GaP nanowires seeded by Pd nanoparticles**.**

3.3 Gallium Phosphide Nanowires

The exploration of GaP nanowires as nanocatalyst supports for nanoparticles was initiated by our research group [81], recognising their potential to offer mechanical stability, biocompatibility, enhanced nanoparticle exposure, and possible Pd-Ga synergy effects.

GaP nanowires are typically grown from Au nanoparticles due to their versatility in a wide range of Ga concentrations and mild temperatures required to ensure VLS

growth, resulting in straight nanowires. On the other hand, using Pd as seed particles is more restricted as high growth temperatures and Ga concentrations are required to promote VLS nanowire growth. These differences can be observed from the Au-Ga and Pd-Ga phase diagrams (Figure 3.4). For instance, at temperatures below 600 °C, for Au-Ga, concentrations as low as 20 at.% Ga may promote VLS growth, whereas for Pd-Ga, concentrations above 50 at.% Ga would be needed.

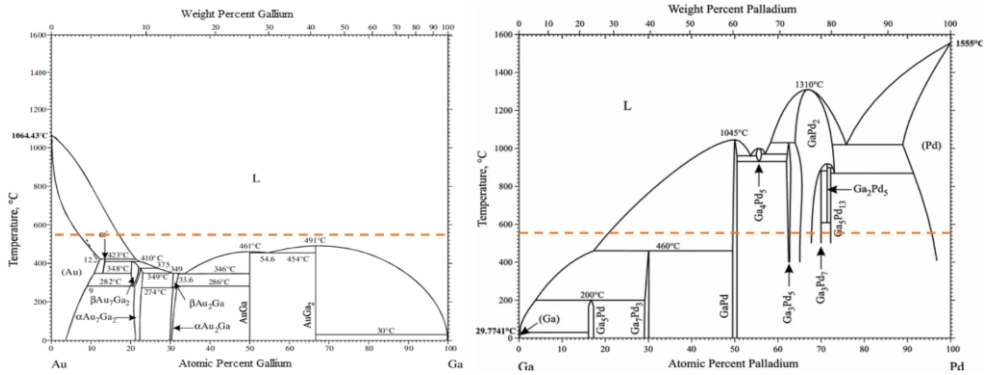

Figure 3.4. Equilibrium phase diagrams of a) Au-Ga and b) Pd-Ga. A wider range of mild temperatures ensures an Au-Ga liquid phase, unlike Pd-Ga, which requires either high temperature or high Ga concentrations.

Au-seeded GaP nanowires

In this thesis, as detailed in **Paper III**, two types of GaP nanowires seeded by Au nanoparticles of 10 nm diameter were grown: thin N-type (N-NWs) and thick K-type (K-NWs) nanowire morphologies. It is well established that growth parameters, including temperature, time, and V/III ratio, directly influence the resulting morphology of the nanowires. Accordingly, N-NWs and K-NWs were grown under distinct conditions: V/III ratios of 110 and 196 and growth temperatures of 540 °C and 550 °C, respectively.

Microscopy characterisation revealed morphological differences between these nanowires grown along $[\bar{1}\bar{1}\bar{1}]$ / $[00\bar{1}]$ directions on (111)B GaP wafers (Figure 3.5). A pronounced tapering observed in K-NWs is attributed to both elevated growth temperature and high V/III ratio. High temperature promotes precursor competition between the adatoms landing on the nanowire sidewalls and the wafer surface. This competition reduces adatom diffusion towards the particle-nanowire interface, favouring material deposition along the sidewalls. Likewise, high V/III ratios further enhance radial growth when the sidewall deposition depletes group III, thus reducing adatoms available for axial growth.

An evaluation of the crystal structure of the GaP nanowires through TEM and HRTEM reveals distinct structural characteristics. In the middle to lower regions, N-NWs predominantly exhibit wurtzite (WZ) structure with stacking defects, while K-

NWs display a mix of WZ, stacking defects, and zinc blende (ZB) segments. As the nanowires narrow to ~10 nm diameter near the tips, N-NWs maintain a WZ structure, while K-nanowires exhibit segments of both WZ and ZB structures. Notably, both nanowire types display stacking fault-free WZ structures near their tips, with N-NWs featuring a significantly longer defect-free segment (235 ± 95 nm) than K-NWs (36 ± 19 nm), where a defect-free WZ structure possesses lower surface energy than the same structure containing multiple stacking faults [35]. Although K-NWs have a longer growth time (20-28 minutes) than N-NWs (7-15.5 minutes), the extended defect-free WZ regions in N-NWs likely arise from growth conditions such as reduced group V concentration, consistent with prior studies on III-V nanowires [82].

These findings highlight the complex interplay between growth parameters and resulting nanowire crystal structure, offering insights into tailoring nanowire properties for specific applications.

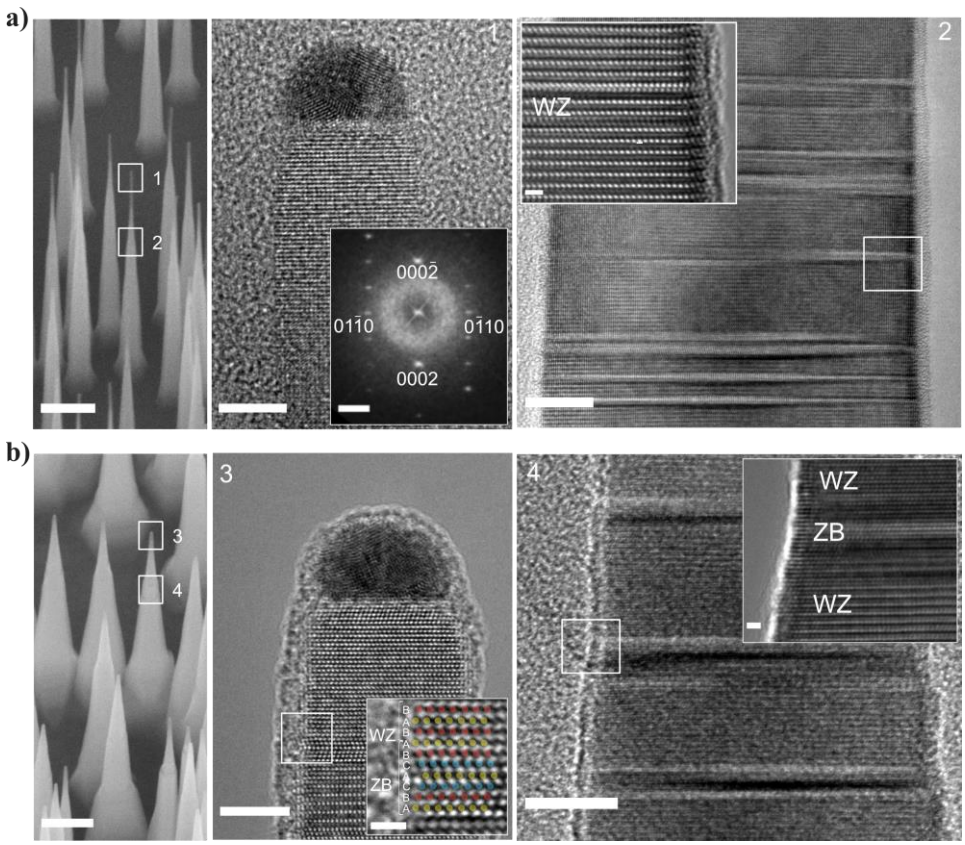

Figure 3.5. GaP nanowires seeded by Au NPs of 10 nm diameter: N-type (a) and K-type (b) nanowires. 30° tilted view SEM micrographs (left), TEM (middle) and HRTEM (right).

Pd-seeded GaP nanowires

Given that Pd nanoparticles are the catalysts of primary interest, an innovative approach was adopted to grow nanowires using Pd as seed particles. However, high-temperature limitations require a shift towards high Ga concentration, i.e., a low V/III ratio. To address this challenge, it was possible to grow straight ⟨111⟩B GaP nanowires using Pd nanoparticles of 10, 20, and 40 nm diameter, where growth conditions were optimised to a V/III ratio of 1.3 and 560 °C, ensuring a kinetic-limited NW growth, following a VLS mechanism.

These Pd-seeded GaP nanowires showed a tapered morphology. TEM revealed a high-contrast Pd-Ga particle at the tip of the nanowire. HRTEM of the middle to lower regions of the nanowires exhibited predominantly multiple-twinned zinc blende (ZB) crystal structure, where the number of stacking faults decreases with increasing nanowire diameter (Figure 3.6).

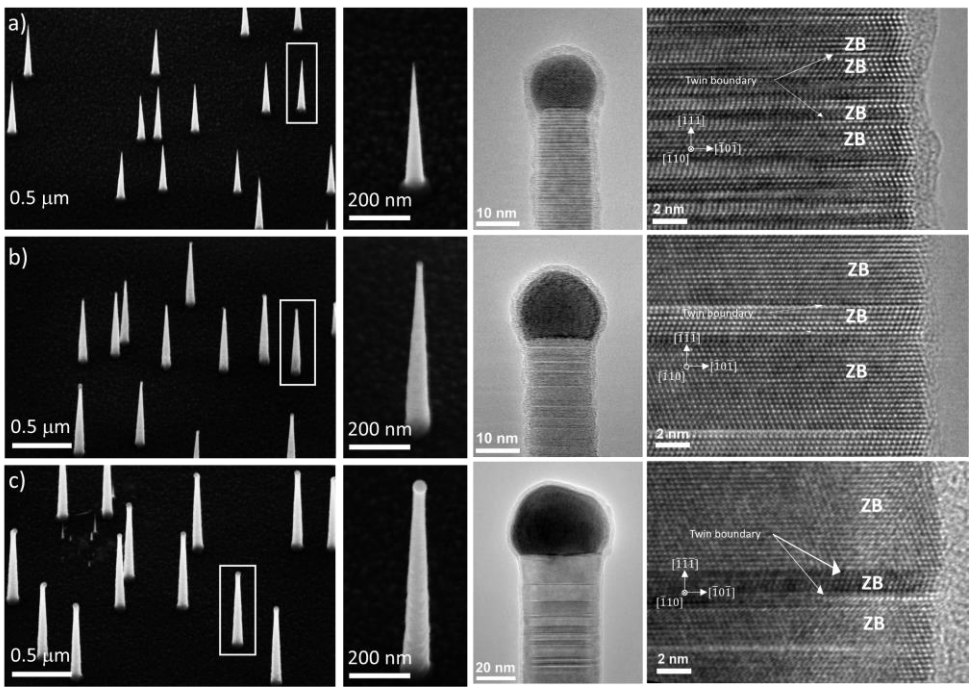

Figure 3.2. SEM (left), TEM (middle), and HRTEM (right) micrographs along the [$\bar{1}10$] zone axis of ⟨111⟩ GaP nanowires grown at 560 °C and a V/III ratio = 1.30 seeded by Pd NPs of a) 10 nm, b) 20 nm, and c) 40 nm diameter. The zoomed-in views of the squared regions are presented in the second column.

3.4 Branch Growth

The transition from 1D to 3D nanostructures in nanocatalysts offers increased surface area and more exposure to Pd nanoparticles. Thus, the branch growth approach consisted of depositing 10 nm Pd nanoparticles on pre-grown core GaP nanowires (Figure 3.7 a, b, c), followed by a second growth phase at the same growth condition as the core nanowires for 10 seconds (Figure 3.7 d, e, f). The results showed that branches grown along the three symmetry-related ⟨111⟩ directions, as has previously been reported for branched GaP nanowires [83]. Twining on the core nanowires causes a 60° rotation of the (111) plane of the core nanowire, causing the branches to grow predominantly on the six facets of the $\{\bar{1}\bar{1}2\}$ and $\{11\bar{2}\}$ family planes (Figure 3.7 g, h, i) [83, 84]. Branch growth initiated before nanoparticle-catalysed growth on the wafer surface, likely due to lower surface energy on core nanowire sidewalls. The growth rate of branches (0.49 ± 3 μm.minute^{-1}) was significantly lower than the core NW growth rate (0.88 μm.minute^{-1}), indicating intense competition for precursor materials between the branches, the sidewalls of the cores, and the core tips during branch growth.

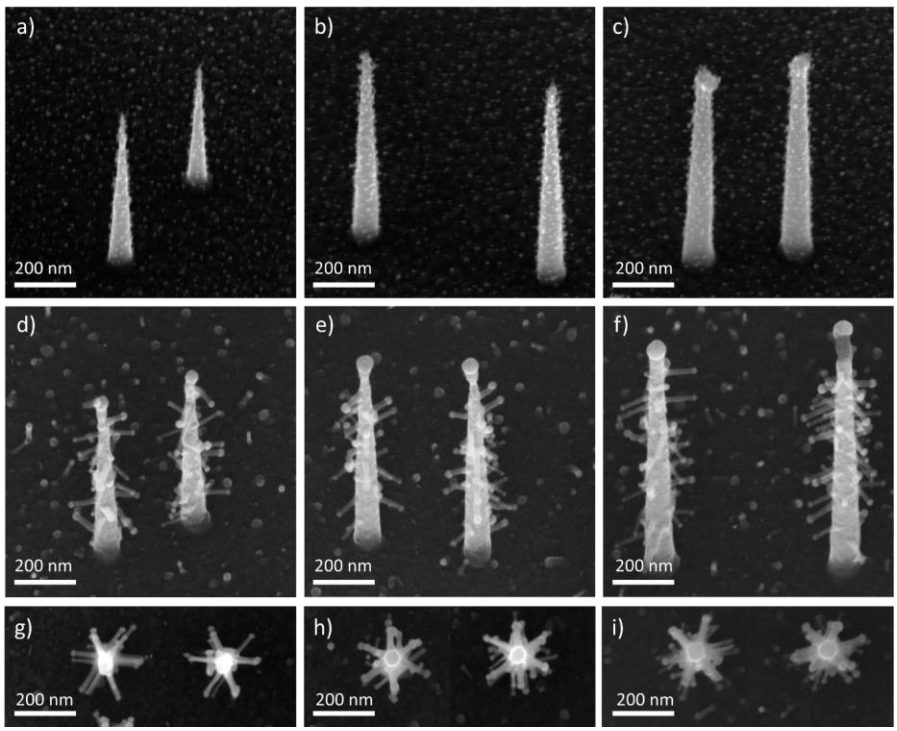

Figure 3.7. SEM micrographs of a second generation of 10nm-Pd NPs for concentrations of 700 particles.μm^{-2}deposited on GaP nanowires seeded by a) 10nm, b) 20nm, and b) 40nm-Pd NPs and their corresponding d), e), and f) branched GaP nanowires after growth during 10 seconds. The SEM micrographs of g), h), and i) correspond to the top views of branched GaP nanowires. The SEM stage is tilted 30^{O} for a) to f).

In addition, TEM and HRTEM (Figure 3.8) revealed that stacking faults extended smoothly along the branches, maintaining structural continuity regardless of growth direction, i.e. ⟨111⟩ and ⟨110⟩ directions. Likewise, the branches preserve the nanowire core stacking faults independently of the branch growth direction. Compositional analysis using STEM-EDX scan profiles showed a similar composition between the tips of the core nanowires and the tips of the branches. The estimated Pd:Ga atomic ratio of 1:1 on the seed nanoparticle suggests the presence of a PdGa phase. As mentioned above, this PdGa phase has been investigated as a catalyst for the selective hydrogenation reaction of acetylene [85].

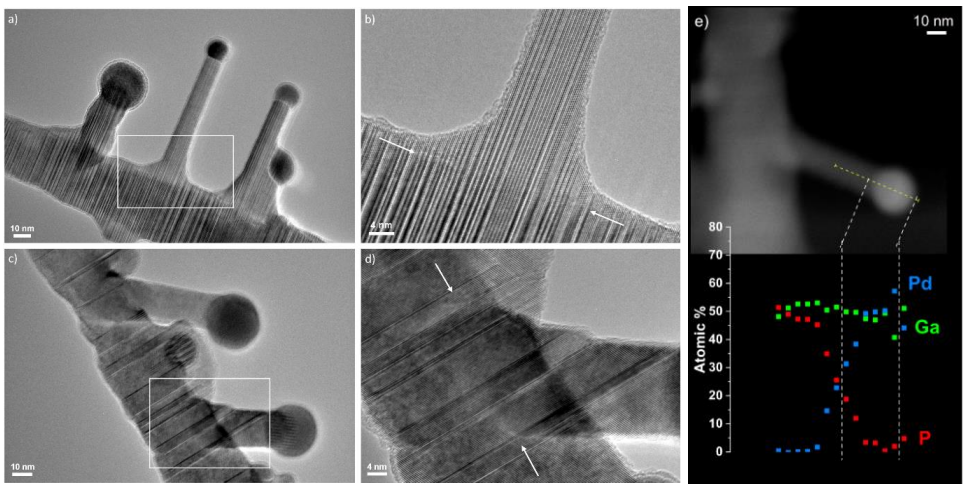

Figure 3.8. TEM (a, c) and HRTEM (b, d) images of branched GaP NWs. The position of b and d are delimited by the squared areas shown in a and c. In e) STEM (top) and EDX atomic composition (bottom) of a branch.

3.5 Au-seeded Core Nanowires and Pd-seeded Branches

A hybrid approach combining Au-seeded core nanowires and Pd-seeded branch growth was explored to obtain nanotrees with improved yield of straight nanowires, providing better mechanical stability for the nanocatalysts.

GaP core nanowires were initially grown using 10 nm Au nanoparticles under the same condition as for the N-NWs (V/III of 110 at 540 °C, density of 20 μm^{-2}). Subsequently, 10 nm Pd nanoparticles were deposited on the sidewalls of the core nanowires at a density of 1000 μm^{-2} using the spark ablation setup (Figure 2.4). Branch growth was then performed in the MOVPE (CCS) following a two-step PH_3 variation in concentration: 1.84 x 10^{-3} molar fraction for the first 5 seconds to ensure nucleation and straight branch growth. In the second step, PH_3 was increased until reaching 3.7 x

10^{-3} (Figure 3.9 a) and 5.0 x 10^{-3} (Figure 3.9 b) during 15 and 10 seconds, respectively, to deplete the excess Ga at the branch tips.

SEM micrographs of these nanotrees (Figure 3.9) showed straight core nanowires with kinking near the Au-Ga tip, attributed to excess Ga causing length extension during the branch growth process. A similar effect of the branches presented in the previous section was observed here, i.e., branch growth predominantly on the six facets of the $\{\bar{1}\bar{1}2\}$ and $\{11\bar{2}\}$ family planes and no observable nanoparticle-catalysed growth on the wafer surface. Although the PH_3 concentration was increased by 35% (from 3.7 x 10^{-3} to 5.0 x 10^{-3}) in the second growth step, no significant differences were observed between these nanotrees besides longer branches (for those with a total growth duration of 20 seconds), which suggests a group III-limited branch growth.

Further characterisation through TEM and STEM/EDX is necessary to elucidate the crystal structure of these branches and fully understand the hybrid growth mechanism.

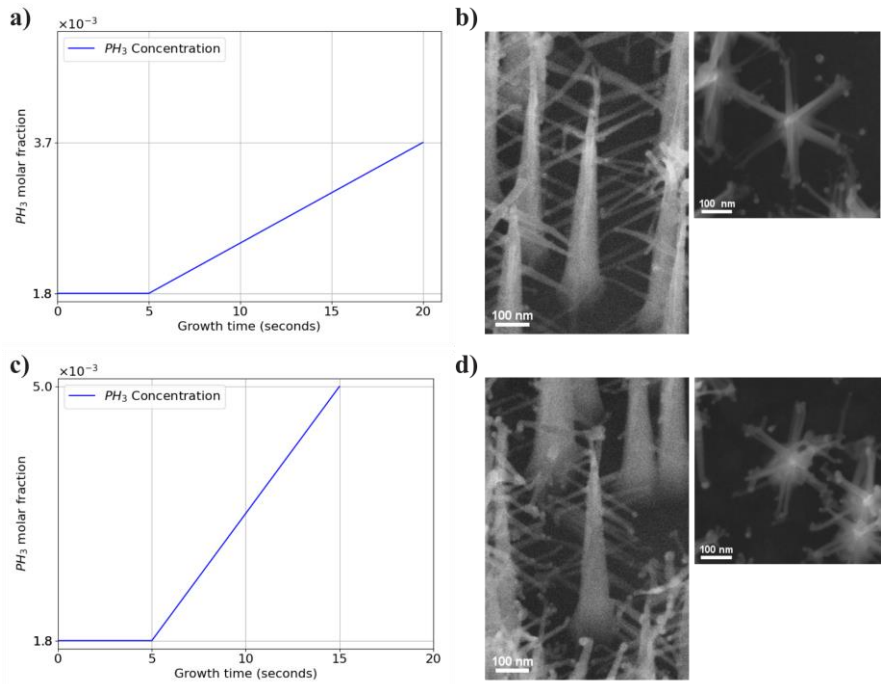

Figure 3.9. a),c) PH_3 molar fraction profile for branch growth b),d) SEM micrographs of branched GaP NWs. The core GaP nanowires were grown from Au seed particles (N-NW type) and the branches from Pd seed particles. The last column shows the top view of the branched nanowires.

4 Nanocatalyst Fabrication

The proper design and fabrication of heterogeneous catalysts are crucial for developing efficient and sustainable chemical processes. Optimised catalyst features can enhance reaction kinetics and improve catalytic performance for specific applications.

This chapter details the fabrication steps of each set of nanocatalysts using spark ablation and MOVPE techniques.

4.1 Modular Nanocatalyst Fabrication

Pd-based nanocatalysts were fabricated using the techniques detailed in Chapters 2 and 3, namely, spark ablation for nanoparticle generation and MOVPE for nanowire and branch growth, using chips of 8 mm x 8 mm (111) B GaP wafers. Each set of nanocatalysts (Table 4 1) involved depositing randomly distributed (size and non-size selected) catalytic nanoparticles at a concentration of 1000 μm^{-2}.

Table 4-1. Fabrication conditions of Nanocatalysts

Group	Nanocatalyst	Pd NP size [nm]	Pd NP density [μm^{-2}]	Support
Pd-Ga nanoparticles	Pd-Ga_1	All sizes	1000	(111)B GaP
	Pd-Ga_3			
	Pd-Ga_5			
Pd nanoparticles supported by GaP nanowires	N-20	10	1000	N-NW-20
	N-40			N-NW-40
	K-20			K-NW-20
	K-40			K-NW-40
Nanotrees	NT-20	10	1000	N-NW-20
References	Pd NPs_A	All sizes	1000	(111)B GaP
	Pd NPs	10	1000	(111)B GaP
	-	-	-	(111)B GaP

4.2 Pd-Ga Nanoparticles

Three nanocatalysts comprised of non-size selected Pd-Ga nanoparticles were produced, following the combined fabrication approach with spark ablation and in-flight decomposition of TMGa (section 2.5) at flow rates of 1, 3, and 5 sccm, corresponding to TMGa molar fractions of 3.7 x 10^{-5}, 11.2 x 10^{-5}, and 18.6 x 10^{-5}, respectively, sintered at 900 °C. The high density of Pd-Ga nanoparticles randomly deposited on (111)B GaP wafers resulted in some particle aggregation without affecting the individual particle morphology (Figure 4.1).

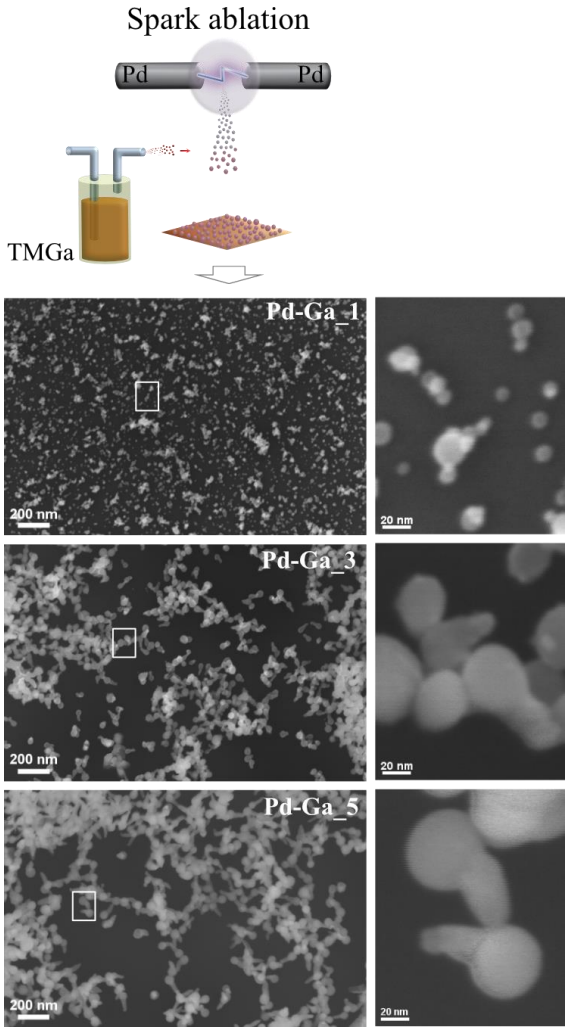

Figure 4.1. Pd-Ga nanoparticles produced through the combined approach spark ablation and injection of TMGa at flow rates of 1, 3, and 5 sccm, namely Pd-Ga_1, Pd-Ga_3, and Pd-Ga_5, respectively, and sintered at 900 °C. The zoomed-in views of the squared regions are presented on the right.

A reference for this nanocatalyst group is non-selected pure Pd nanoparticles sintered at 900 °C and deposited on (111)B GaP wafers at the same estimated particle concentration of 1000 μm^{-2} (Pd NPs_A). An additional reference of a blank (111)B GaP wafer was used for comparison purposes in wettability analysis (Chapter 5).

4.3 Pd Nanoparticles Supported by GaP Nanowires

Four nanocatalysts, consisting of Au-seeded GaP nanowires, were produced and decorated with 10 nm Pd nanoparticles. The fabrication process started with generating 10 nm Au nanoparticles via the evaporation/condensation aerosol method (section 2.1) using two DMAs (upstream and downstream of the sintering furnace) for precise control over particle concentration. The high-temperature furnace was at ~1520 °C for Au evaporation, and the sintering furnace was at 600 °C to reach particle compaction. The Au nanoparticles were produced in concentrations of 20 and 40 μm^{-2} randomly deposited on GaP (111) B wafers.

These Au nanoparticles were loaded into the MOVPE reactor to grow GaP nanowires (section 3.3). Each nanowire growth recipe adjusted the growth time to attain ~1.5 μm in length. The nanowire supports can be distinguished by their growth conditions, resulting in characteristic tapering, namely thin (N-NWs) and thick (K-NWs) nanowire supports.

Finally, the GaP nanowires were loaded into the SDG, where 10 nm Pd nanoparticles produced through spark ablation and sintered 750 °C were randomly deposited onto the sidewalls of the GaP nanowire supports

The SEM micrographs (Figure 4.2) show that the nanowire supports remain the same upon Pd nanoparticle deposition. The high density of Pd nanoparticle deposition leads to some particle aggregation. Also, these nanocatalysts show some tip-bending for N-20 and N-40 due to the electron beam exposure during imaging, while K-20 and K-40 remain straight.

It is worth noting that K-type nanowire supports of 40 μm^{-2} (K-NW-40) showed variation in nanowire tapering and length across samples, likely due to extended growth times combined with the tapering, density, and random distribution of nanowires.

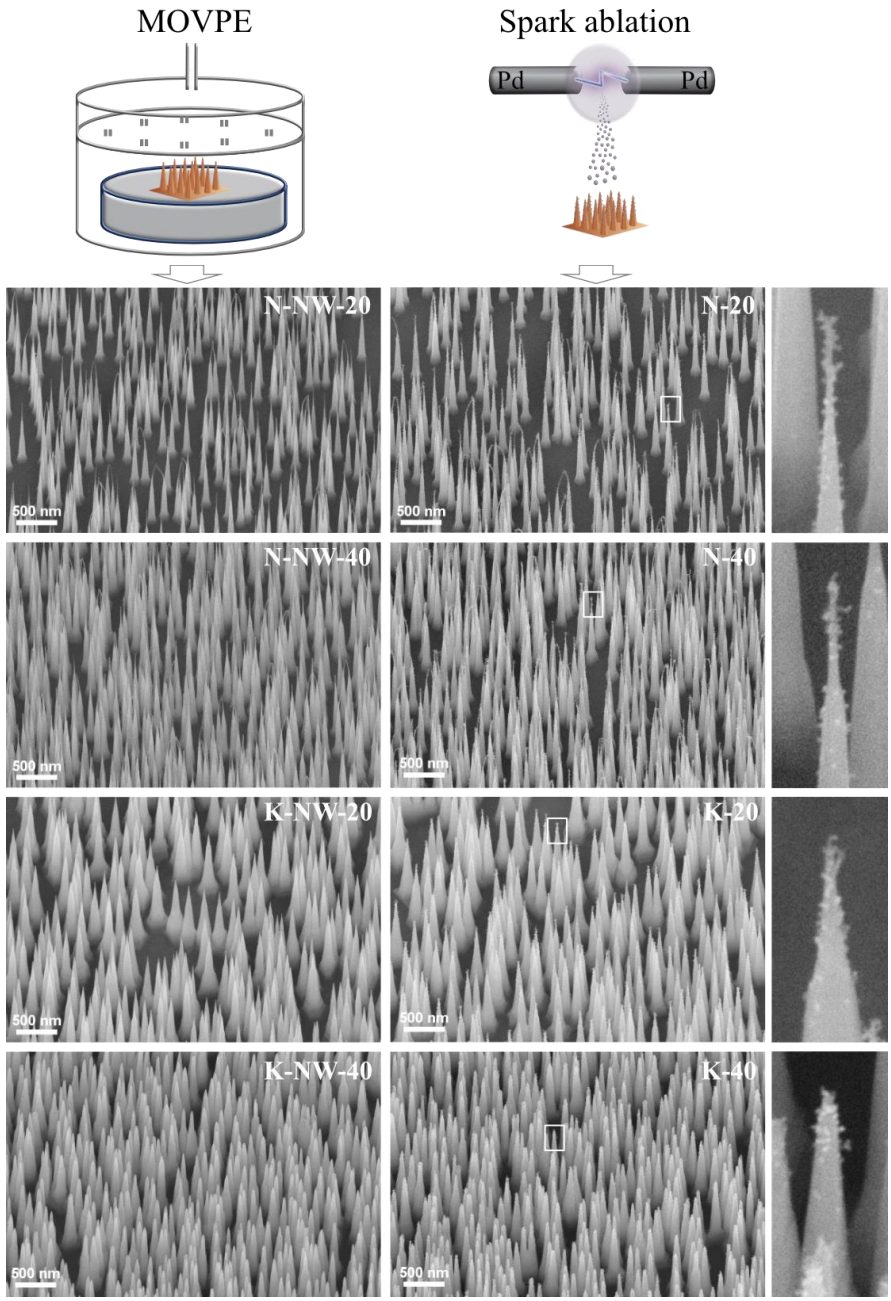

Figure 4.2. Support nanowires (left) and nanocatalysts (middle and right) comprised of nanowires decorated with Pd nanoparticles. The zoomed-in views of the squared regions are presented in the last column.

The regions near and at the nanowire tips are the first to encounter incoming Pd nanoparticles, resulting in a higher concentration than the lower sidewall regions. This preferential deposition occurs due to the enhanced accessibility and exposure of the tips, creating a gradient of nanoparticle density along the nanowire supports.

TEM and HRTEM micrographs show Au-based nanoparticles with higher contrast and spherical lower contrast Pd nanoparticles attached to sidewalls. Most Pd nanoparticles are single crystalline, visible along (111) planes with a 2.2 Å d-spacing, with some polycrystalline particles observed. Crystallinity variation may result from nanoparticle agglomeration during spark ablation (Figure 4.3). Moreover, STEM-EDX showed a mean atomic Ga:P ratio of 1:1, and the Pd nanoparticles remain mostly spherical and attached to the nanowire sidewalls.

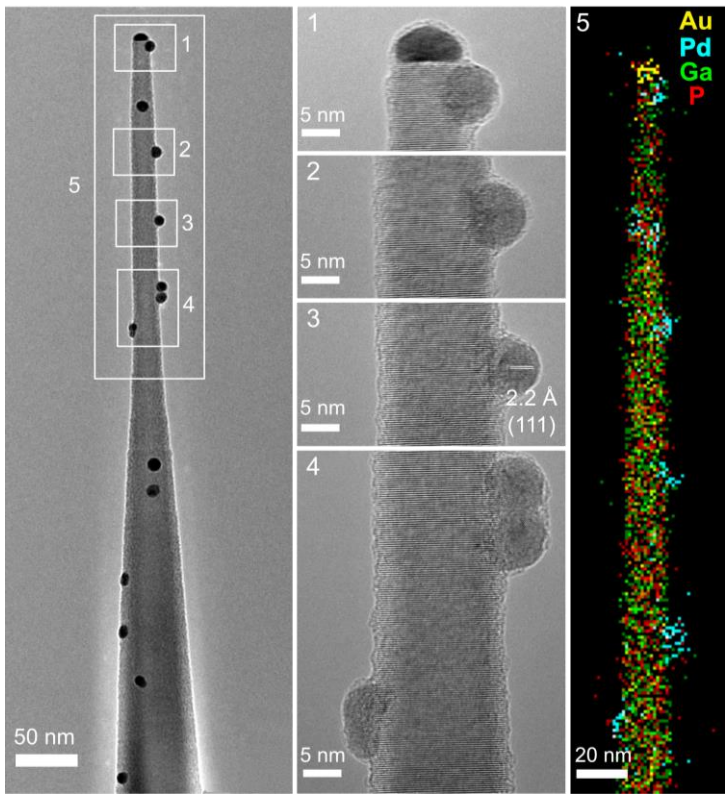

Figure 4.3. Bright field TEM (left), HRTEM (middle), and STEM/EDX mapping (Au, Pd, Ga, and P convoluted signals) of the upper section of a nanocatalyst comprised of NW support with Pd NPs.

4.4 Nanotrees

The nanotree catalyst was produced from Pd-seeded GaP branches grown on the sidewalls of Au-seeded GaP core nanowires (section 3.5), with a concentration of 20 μm^{-2} (N-NW-20). This design, featuring stable and low-density core nanowires may offer superior stability compared to Pd seeded GaP core nanowires. To create these hierarchical branched structures, the previously fabricated N-20 nanocatalysts were loaded again into the MOVPE reactor for branch growth using the 2-step PH_3 variation from 1.84 x 10^{-3} to 5.0 x 10^{-3} molar fraction (Figure 4.4). This additional step results in the formation of branched nanowires, enhancing the overall surface area and creating a more complex structure with the potential for Pd-Ga (from the branch tips) synergetic effects, attractive for Pd-based catalysts.

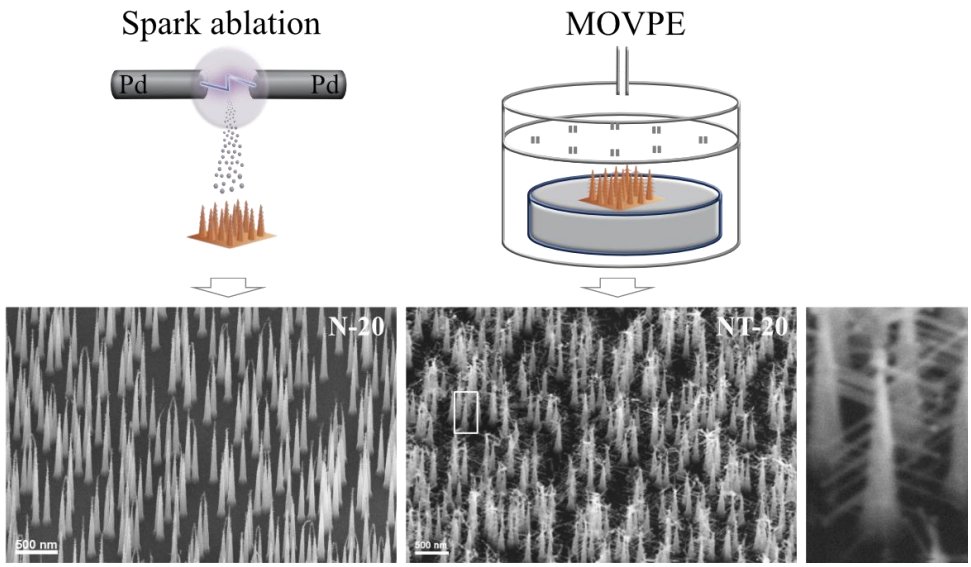

Figure 4.4. Nanotrees (NT-20) comprised Pd-seeded branched nanowires and Au-seeded core nanowires (N-NW-20). The zoomed-in view of the squared region is presented in the last column.

5 Wettability Analysis

Wettability is a critical factor in various industrial processes, including catalysis. The water contact angle provides valuable insights into surface-liquid interactions. For example, contact angle measurements are used in the pharmaceutical industry to formulate drugs with specific dissolution rates. In catalysis, wettability can influence the performance of heterogeneous catalysts by enhancing reactant adsorption, mass transfer, and gas-liquid-solid interfaces. Optimising wettability might enable the design of efficient catalysts.

This chapter presents the basic concepts of wettability, including contact angle and wetting regimes. Subsequently, a wettability analysis was performed across the nanocatalysts fabricated and presented in this thesis.

5.1 Surface Wettability Regimes

Contact angle

Surface wettability can be determined by measuring the contact angle between a liquid droplet and the solid surface, which is readily accomplished using an optical tensiometer. The contact angle describes the surface wettability ranging from superhydrophilic to superhydrophobic surfaces (Figure 5.1).

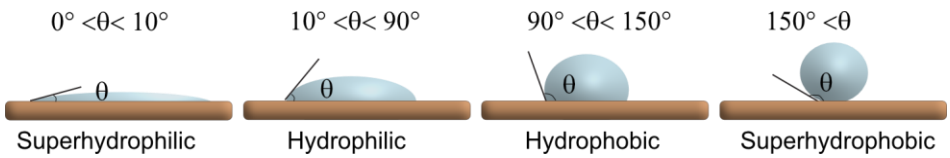

Figure 5.1. Surface wettability based on the contact angle between a liquid droplet and a solid.

The theoretical basis for contact angle is given by the Young equation (Eq. 5.1), which describes the thermodynamic equilibrium with the lowest energy state of the solid, liquid, and gas phase of a droplet:

$$\gamma_{SV} = \gamma_{SL} + \gamma_{LV}.cos\theta_y \qquad \text{Eq. 5.1}$$

where θ_y is the Young contact angle, γ_{SV}, γ_{SL}, and γ_{LV} are the interfacial tensions of solid-vapour (solid surface free energy), solid-liquid, and liquid-vapour, respectively.

Surface wettability regimes

When there is a homogeneous wetting (droplets fully enter the microstructures of a rough surface), the Wenzel regime takes place [86] (Figure 5.2 a), defined by Eq. 5.2:

$$\cos\theta_m = \mathrm{r}.\cos\theta_y \qquad \text{Eq. 5.2}$$

where θ_m is the apparent contact angle experimentally measured, $r = S_a / S_p$ is the surface roughness as a ratio between the actual wetted surface area (S_a) and the projected planar area (S_p).

When there is heterogeneous wetting due to vapour traps (e.g. air) in the valleys of the microstructures of a rough surface, the Cassie-Baxter model is applicable [87, 88]. Two regimes can be observed: Cassie-Baxter I for partial wetting (Figure 5.2 b) and Cassie-Baxter II when there is no wetting of the microstructures (Figure 5.2 c). This model is given by Eq. 5.3:

$$\cos\theta_m = f_1.\cos\theta_y - f_2 \qquad \text{Eq. 5.3}$$

where f_1 and f_2 are the areas of the liquid droplet in contact with the solid and trapped air per unit projected area, respectively. In Cassie-Baxter I $f_1 + f_2 > 1$ and in Cassie-Baxter II $f_1 + f_2 = 1$.

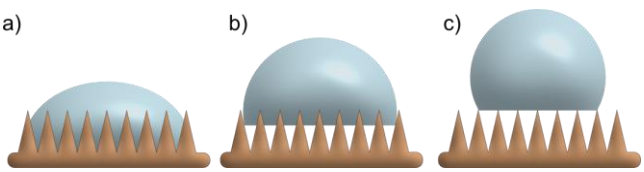

Figure 5.2. Schematic diagrams of three wetting regimes on rough surfaces: a) Wenzel regime, b) Cassie-Baxter I regime, and c) Cassie-Baxter II regime.

5.2 Surface Wettability of Nanocatalysts

Surface wettability in H_2O was measured for the nanocatalysts, and references shown in Table 4-1. Three main nanocatalyst groups were evaluated:

1. Pd-Ga nanoparticles: Pd-Ga_A, Pd-Ga_1, Pd-Ga_3, and Pd-Ga-5 (from **Paper II**).
2. Pd NPs supported by GaP nanowires: N-20, N-40, K-20, and K-40 (from **Paper III**).
3. Nanotrees (NT-20), consisting of Pd-seeded GaP branches grown on Au-seeded GaP core nanowires (N-NW-20 type).

A blank (111) B GaP wafer and Pd nanoparticles (10 nm and all sizes) were used as references.

Pure Pd nanoparticles (all sizes, Pd NP_A) and the (111)B GaP wafer exhibited hydrophobic and hydrophilic wettability with contact angles of 102.5 ± 0.5° and 74.7 ± 0.1°, respectively. This indicates that Pd nanoparticles significantly influence the surface wettability of the (111)B GaP wafer, shifting towards a hydrophobic behaviour.

Pd-Ga nanoparticles showed comparable hydrophobic wettability with contact angles between 98.6° ± 0.4° and 106.3° ± 2.9°, like pure Pd NPs (Figure 5.3 a). This suggests a predominant influence of Pd over Ga content. The contact angle slightly increases with Ga content, and all these nanocatalysts fall within the Cassie-Baxter regime. The observed hydrophobicity may primarily arise from a variation in particle size across the nanoparticles, with a lesser contribution from the surface roughness of the Pd-Ga particles and particle growth (only visible for Pd-Ga_3 and Pd-Ga-5).

On the other hand, the wettability of pure 10 nm-Pd nanoparticles, which showed a contact angle of 80.3° ± 2.9°, indicates a slight influence in reducing the hydrophilicity of (111)B GaP wafer.

The surface wettability of Pd nanoparticles supported by GaP nanowires can be effectively tuned by adjusting fabrication conditions. Indeed, nanocatalyst morphology induced a significant shift in wetting behaviour with respect to their references (Figure 5.3 b), i.e., N-20 and N-40 displayed hydrophobic wettability with contact angles of 115.3° ± 0.1° and 119.1° ± 0.1°, respectively, whereas K-20 and K-40 exhibited hydrophilic properties with contact angles of 50.4° ± 0.4° and 33.4° ± 1.4°, respectively. The hydrophobic nature of N-20 and N-40 nanocatalysts aligns with the Cassie-Baxter model, where trapped air pockets in surface irregularities enhance hydrophobicity. Conversely, K-20 and K-40 nanocatalysts exhibit wetting behaviour consistent with the Wenzel model, where liquid fully wets the rough surface. The transition between these regimes (Cassie-Wenzel transition) demonstrates the dynamic nature of wetting on the nanowire supports. The minimal variation in contact angle within each nanocatalyst group (20 μm^{-2} and 40 μm^{-2}) indicates that wettability depends more on nanowire morphology, determined by fabrication conditions, than on areal density.

TEM studies reveal that crystal structure differences may be a key factor. The higher density of stacking defects in K-20 and K-40 nanocatalysts could enhance wettability, while the stacking fault-free regions and predominantly wurtzite structure (lower surface energy) in N-20 and N-40 may contribute to their hydrophobic behaviour, in addition to the nanowire tapering and air trapping effects.

Finally, the nanotrees (NT-20) exhibit the highest hydrophobicity among all the nanocatalysts, with a contact angle of 136.4° ± 0.6°. The wettability in the Cassie-

Baxter regime of these nanotrees suggests a combined effect from air-pocket formation in the spaces between nanowires and branches, the morphology of the core nanowires, and the Pd-Ga alloy at the branch tips. Further characterisation is essential to determine the influence of the nanotree morphology, including its crystal structure, on this hydrophobic behaviour.

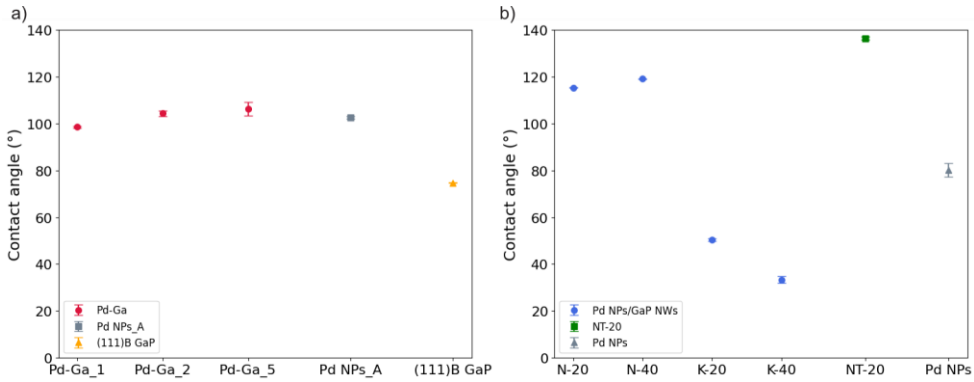

Figure 5.3. Wettability in H_2O of a) Pd-Ga nanocatalysts (Pd-Ga_1, Pd-Ga_3, and Pd-Ga_5), non-size selected Pd nanoparticles of 1000 μm^{-2} (Pd NPs_A) and (111)B GaP wafer; and b) Pd nanoparticles supported by GaP nanowires (N-20, N-40, K-20, and K-40).), nanotrees (NT-20), and 10 nm Pd nanoparticles of 1000 μm^{-2} (Pd NPs).

6 Catalytic Assessment

How good a catalyst is can be determined by assessing its performance and suitability for specific applications. This catalytic evaluation helps to optimize reactions, reduce waste, and improve yields.

This chapter explores the catalytic performance of Pd-based nanostructures in hydrogenation reactions. We begin by introducing key metrics in catalysis, including activity and selectivity, followed by a description of the benchmark reaction - the partial hydrogenation of phenylacetylene to styrene [89, 90]- which serves as a model system for evaluating catalytic activity. The selective hydrogenation of alkynes has significant industrial applications, from vitamin synthesis to polymer production. The chapter then delves into the catalytic performance of our engineered nanocatalysts, comparing their efficiency to commercial alternatives.

6.1 Performance Metrics for Catalysis

Activity and selectivity

In heterogeneous catalysis, important catalytic performance metrics include turnover frequency (TOF) and catalytic selectivity (S).

> TOF, also referred to as true turnover rate and site time efficiency, measures the catalytic activity of a catalyst and it is defined as the ratio of product molecules per unit of time [91], according to Eq. 6.1:

$$\mathrm{TOF} = \frac{Number\ of\ moles\ produced}{Number\ of\ moles\ of\ catalyst.time}\ [s^{-1}] \qquad \text{Eq. 6.1}$$

Catalytic selectivity refers to the ability of a catalyst to promote a specific reaction pathway relative to all possible reaction routes, i.e., the catalyst's ability to favour the formation of a desired product over competing by-products. Selectivity can be quantified as the ratio of a desired product to the undesired product, and it is given by Eq. 6.2:

$$\mathrm{S} = \frac{Number\ moles\ of\ desired\ product}{Number\ of\ moles\ of\ undesired\ product} \qquad \text{Eq. 6.2}$$

Mass and moles of Pd

To estimate the catalytic metrics, the mass and number of moles of Pd are required. The nanocatalysts were produced on chips of 8 mm x 8 mm at 1000 Pd μm^{-2} which concentrates 6.4 x 10^{10} Pd nanoparticles. Considering monodisperse 10 nm Pd nanoparticles, an average Pd density of 12.02 $kg.m^{-3}$, and a molar mass of 106.42 $g.mol^{-1}$, the resulting mass and number of moles are shown in Table 6-1.

Table 6-1. Properties of Pd nanoparticles

	1 Pd NP	1000 Pd NP.μm^{-2}
Nr. of NPs	1	6.4 x 10^{10}
Mass (kg)	6.294 x 10^{-21}	4.028 x 10^{-10} (0.4 μg)
Volume (m^3)	5.236 x 10^{-25}	3.351 x 10^{-14}
Nr. of moles of Pd	5.914 x 10^{-20}	3.785 x 10^{-9}

6.2 Benchmark Reaction

The hydrogenation reaction evaluated in this thesis is the metal-catalysed semi-hydrogenation of alkynes to cis-alkenes. This type of reaction is essential in producing fine chemicals in the synthesis of pharmaceutical and natural products. Achieving high selectivity for cis-alkenes while preventing over-hydrogenation to alkanes presents a notable challenge in catalysis. Ongoing research aims to enhance catalyst efficiency and selectivity, exploring alternatives to traditional Pd-based systems.

In the production of styrene, a commodity of high value in the chemical industry, phenylacetylene is an undesirable byproduct, and Pd-based catalysts are suitable for recycling phenylacetylene to produce more styrene [89]. Therefore, the benchmark for catalytic evaluation is the partial hydrogenation of phenylacetylene to styrene (Figure 6.1). The Pd-based nanocatalysts presented in this thesis offer significant potential as a viable alternative to the commercial Lindlar catalyst (Pd-Pb/ $CaCO_3$), which despite its effectiveness in selective hydrogenation of alkynes to cis-alkenes, has several disadvantages, including toxicity (Pd particles poisoned with lead and quinoline) [92], sensitivity (excessive hydrogenation under inadequate control of hydrogen pressure and reaction time) [93], high cost (~18 SEK/g), and need for additives (e.g., amines)[94], among others.

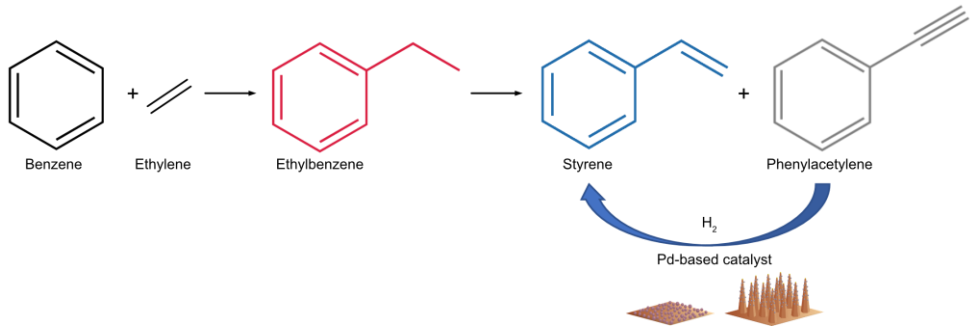

Figure 6.1. Typical hydrogenation reaction to produce styrene. The byproduct phenylacetylene can be recycled via a semihydrogenation reaction using a Pd-based catalyst.

6.3 Nanocatalyst Performance Assessment

Experimental setup

The nanocatalyst chips (up to 4 simultaneously) are placed facing upwards in 5 mL vials. Each vial is sealed, evacuated, and filled with H_2 gas (1.05 bar). After 15 min, the alkyne (10 μL, 0.09 mmol of phenylacetylene), bicyclohexyl (25 μL) (internal standard) and the solvent (2.0 mL of acetone) were added, and H_2 gas was bubbled through the solution for 30 s. A Schlenk line connected to a H_2-cylinder maintains constant pressure throughout the reaction (Figure 6.2). The vessel is shaken at 150 rpm using an orbital shaker during the process. Reaction progress is monitored via gas chromatography, measuring concentrations of phenylacetylene, styrene, and ethylbenzene.

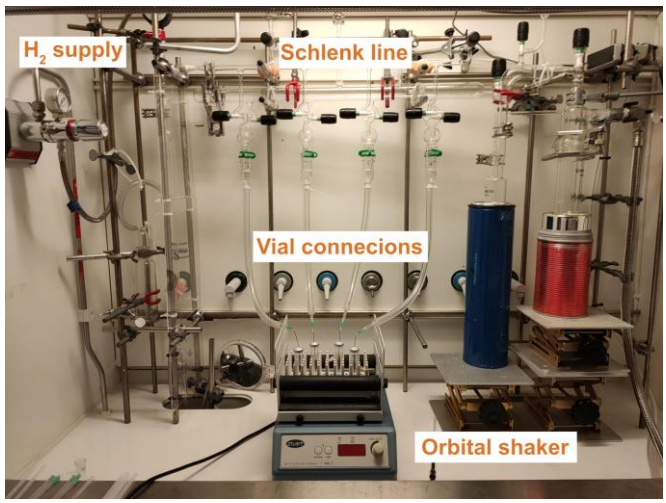

Figure 6.2. Catalysis setup for partial hydrogenation of phenylacetylene to styrene.

Pd-Ga nanoparticles:

Preliminary catalytic results for the Pd-Ga nanocatalysts revealed that Ga concentration plays a critical role in the catalytic performance of the partial hydrogenation of phenylacetylene to styrene (Figure 6.3). After the first 22 hours, phenylacetylene was transformed into the desired styrene and the byproduct ethylbenzene. Pd-Ga_1 exhibited higher catalytic activity than pure Pd nanoparticles (Pd NP_A) with a styrene formation of ~28.74 mmol.L^{-1} (Figure 6.3 a). and ~19.22 mmol.L^{-1} (Figure 6.3 b)., respectively. The catalytic activity is 49.5% higher for Pd-Ga_1 than Pd NP_A, suggesting that a low Ga concentration boosts catalytic performance by limiting overhydrogenation, which leads to ethylbenzene formation. It is worth noting that the maximum styrene formation occurs before 22 hours, i.e., before any significant ethylbenzene is detected for both Pd-Ga_1 and Pd NPs_A.

At the same reaction conditions. Pd-Ga_3 and Pd-Ga_5 showed negligible catalytic activity (Fig A1 in Appendix A), indicating that excess Ga significantly hinders catalytic efficiency. Further investigation into the optimal Ga concentration range could enhance catalyst designs for specific hydrogenation reactions.

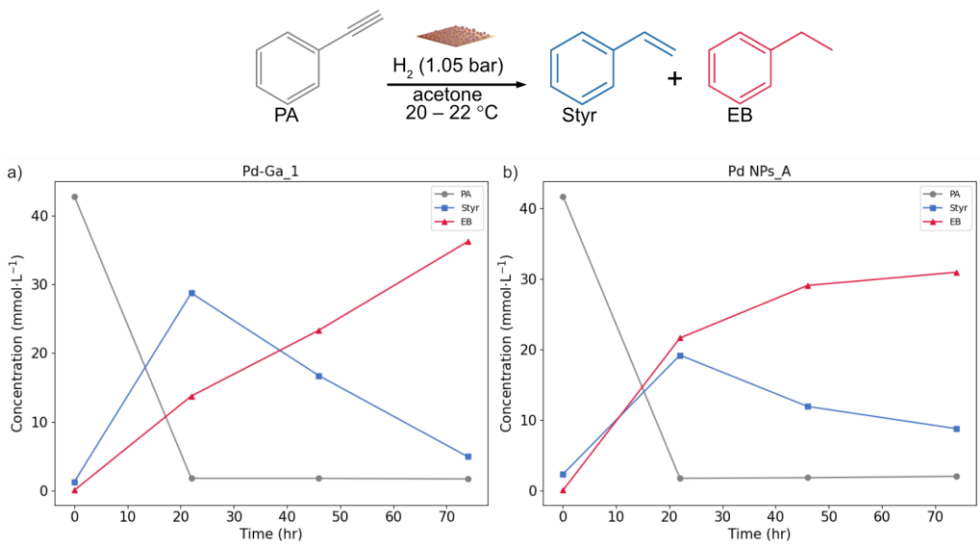

Figure 6.3. Concentration (mmol/L) of phenylacetylene (PA), Styrene (Styr) and ethylbenzene (EB) formation over time for Pd-based nanocatalysts a) Pd-Ga_1 and b) Pd NPs_A, during a partial hydrogenation reaction of PA to Styr.

A comparison of the nanocatalyst Pd-Ga_1 before and after one cycle of a hydrogenation reaction of phenylacetylene to styrene (Figure 6.4) suggests that the nanoparticles remain attached to the wafer without signs of particle growth or

aggregation. Stability tests such as recyclability are essential to ensure the long-term performance and viability of these nanocatalysts.

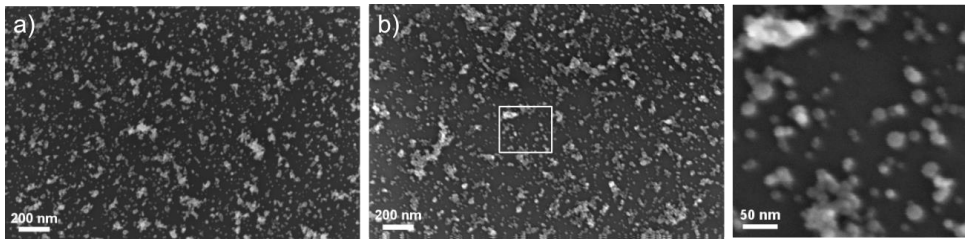

Figure 6.4. Pd-Ga_1 nanocatalysts a) before and b) after one cycle of a hydrogenation reaction of phenylacetylene to styrene. The zoomed-in view of the squared region is presented in the last column.

Pd nanoparticles supported by GaP nanowires

The catalytic performance of the GaP nanowire-supported palladium nanocatalysts revealed significant differences (Figure 6.5). As the concentration of phenylacetylene decreases, styrene forms and each nanocatalyst design shows catalytic activity. After 22 hours of reaction, the styrene formation reached 28.0, 24.4, 18.5, and 15.7 mmol.L^{-1} for N-20, N-40, K-20 and K-40, respectively. Upon further hydrogenation, ethylbenzene starts forming until phenylacetylene is consumed for 120 hours. Interestingly, nanocatalysts supported on N-type nanowires demonstrated superior performance compared to those on K-type nanowires, with the N-20 and K-20 variants showing the highest activity within their respective groups. The enhanced activity observed at lower nanowire densities could be attributed to improved reactant transport within the reaction medium. As for K-40, the variation in catalytic activity may be attributed to the morphological variations across samples affected by the nanowire growth conditions.

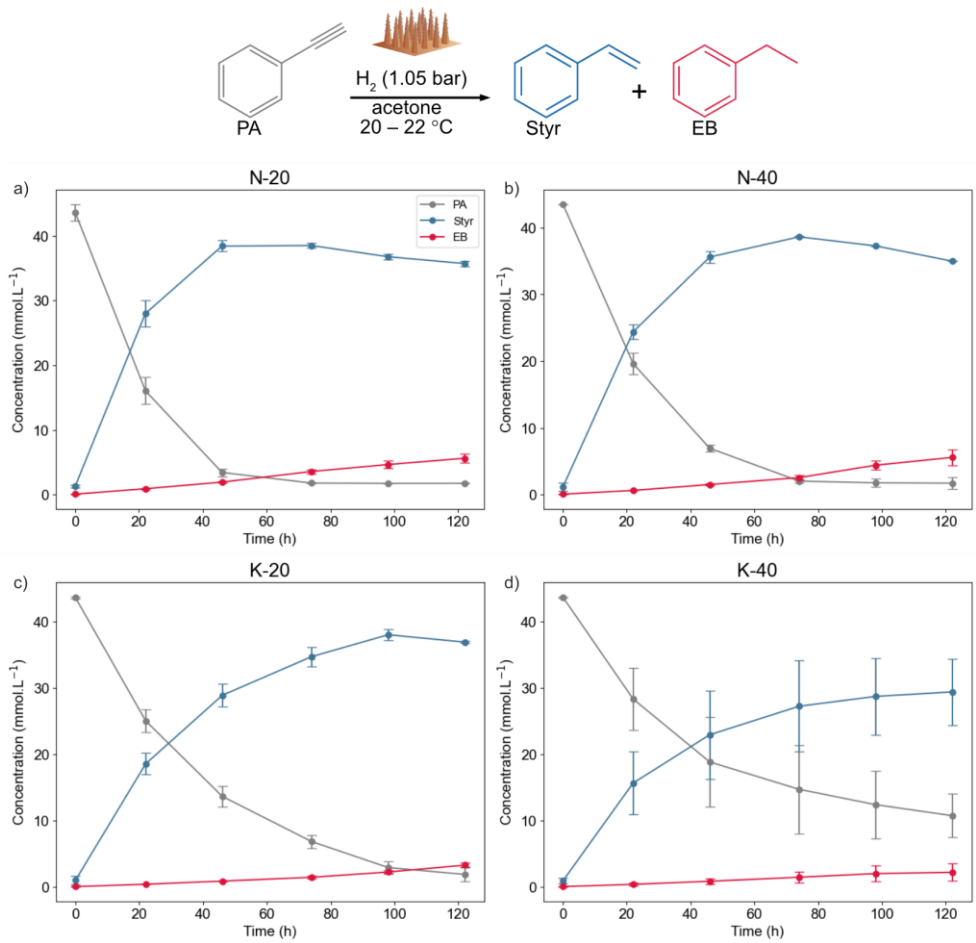

Figure 6.5. Concentration (mmol/L) of phenylacetylene (PA), Styrene (Styr) and ethylbenzene (EB) formation over time for nanocatalysts consisting of Pd nanoparticles supported by GaP nanowires, during a partial hydrogenation reaction of PA to Styr.

The N-20 nanocatalyst was the most catalytically active with a TOF of ~192.9.7 mmol.mol-1.s-1 at ~50% conversion, higher than their counterparts, pure 10 nm-Pd nanoparticles (Pd NPs), and the commercial Lindlar catalyst tested at the same reaction conditions (Figure 6.6 a). Among the nanocatalysts and during the first 22 hours the TOFs are 192.9, 166.9, 126.5, and 107.16 $mmol.mol^{-1}.s^{-1}$ for N-20, N-40, K-20, and K-40, respectively. Moreover, each nanocatalyst exhibited an excellent selectivity for the formation of styrene over ethylbenzene. For example, at ~50 % conversion, the comparable selectivity among the nanocatalysts is ~98:2 (Figure 6.6 b).

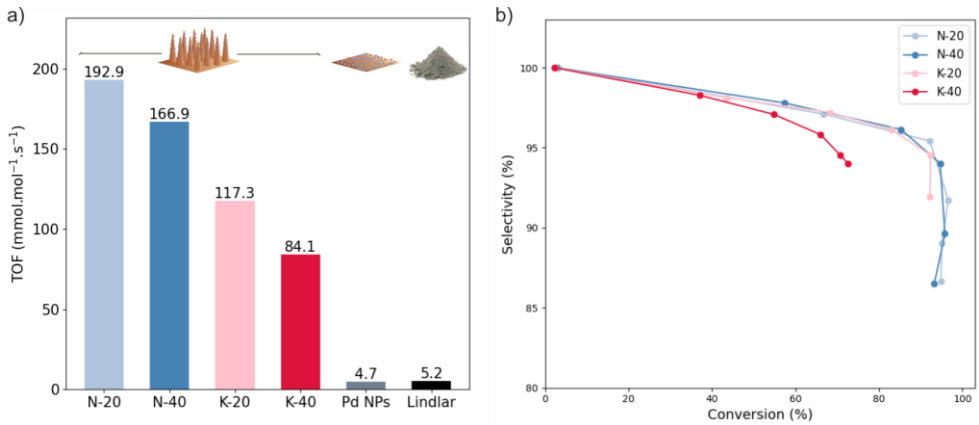

Figure 6.6. a) TOF calculated at ~50% conversion (~10% maximum conversion achieved for Pd NPs) and expressed as formed Styr + EB (mmol) per amount of Pd (mol) per second. b) Selectivity obtained from Styr / EB versus conversion (%)

Since each nanocatalyst contains an identical Pd nanoparticle density of 1000 μm^{-2}, the nanowire support plays a critical role in defining the overall properties and performance of the nanocatalysts. An observed correlation between wettability and catalytic activity suggests that hydrophobic nanocatalysts, i.e., those supported by N-type nanowires, are more effective for this specific reaction, possibly due to the hydrophobic interaction between the phenylacetylene substrate and the catalyst surface over the acetone solvent. However, it is essential to note that the ideal wettability may vary with different substrates or catalytic reactions, as some may benefit from a hydrophilic catalyst surface instead [95]. Therefore, further studies are required to clarify the influence of nanowire support properties on the catalytic performance of these nanocatalysts across various reaction environments.

Finally, after one cycle of a hydrogenation reaction of phenylacetylene to styrene, a visual comparison with the pristine nanocatalysts (Figure 6.7) shows subtle differences. The N-20 nanocatalysts exhibit a tendency for adjacent nanowires to bend and touch at their tips, likely due to their narrow diameter, which makes it difficult for them to remain straight compared to the K-20 nanocatalysts. Additionally, the particles remain attached to the nanowire supports, although some particle aggregation is observed near the upper regions of the nanowires. Therefore, optimising N-type nanowire supports to prevent tip bending and conducting three-phase and recyclability tests for all these nanocatalysts will be essential to determine their long-term performance and viability.

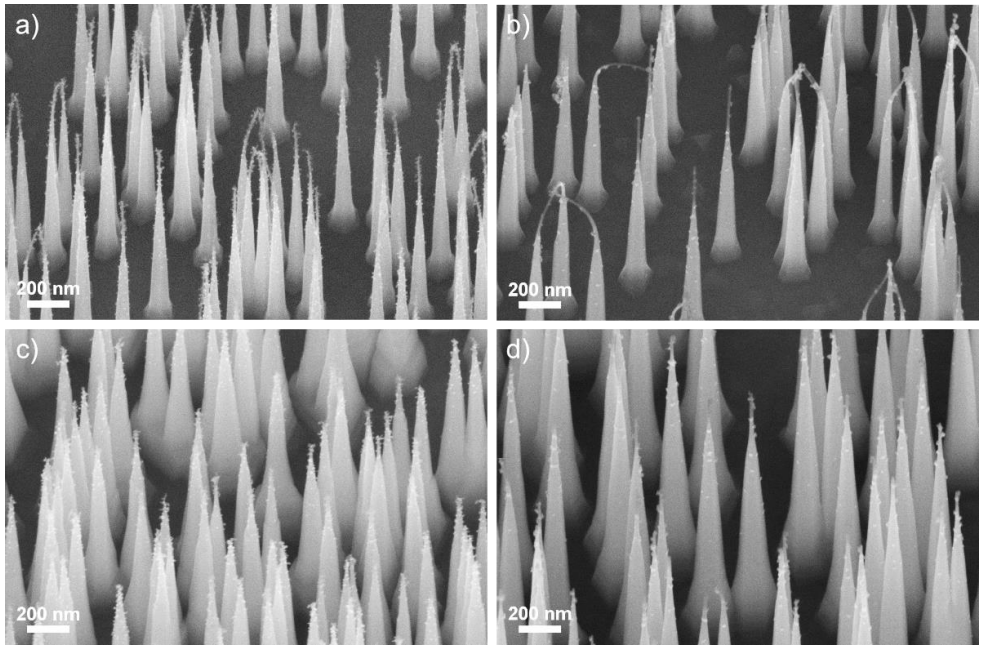

Figure 6.7. a),b) N-20 and c), d) K-20 nanocatalysts a), c) before and b),d) after one cycle of a hydrogenation reaction of phenylacetylene to styrene.

7 Conclusions and Outlook

The work carried out in this thesis focused on the fabrication of Pd-based nanostructures as potential candidates for catalytic applications. From developing simple nanoparticles to complex 3D nanoarchitectures, it was possible to achieve a thorough understanding of the variables governing the design and fabrication of these nanomaterials.

Pd-based nanoparticles for catalysis

The evaluation of various chamber configurations on nanoparticle output, conducted through COMSOL simulations and experimental measurements addressed in **Paper I**, revealed significant differences. When the inlet and outlet of the spark discharge generator (SDG) were positioned closer to the electrodes, the velocity at the electrode gap increased threefold compared to the existing configuration with shorter inlet and outlet inner tubes. This adjustment resulted in substantially higher nanoparticle output and reduced nanoparticle deposition time. These findings highlight the potential for further optimisation of the SDG and underscore the importance of understanding the particle generation process, which is crucial for enhancing the scalability of spark ablation.

The exploration of Pd-based nanomaterials for catalysis led to a challenging, yet promising approach: alloying Pd nanoparticles with low melting point materials such as Ga. This strategy, driven by the unique Pd-Ga synergistic effects on catalysis, was investigated in **Paper II**. The study achieved the production of tuneable Pd-Ga alloys and identified several phase formations by varying TMGa concentration and sintering temperatures, resulting in either Pd- or Ga-rich phases suitable for a variety of catalytic applications. In addition, preliminary hydrogenation reaction tests on these Pd-Ga nanocatalysts revealed that Pd nanoparticles alloyed with low Ga concentrations exhibited enhanced catalytic activity compared to pure Pd nanoparticles. This observation highlights the importance of precise control over phase formation in optimising catalytic performance, demonstrating the potential of tailored Pd-Ga alloy nanoparticles to improve catalytic efficiency in targeted chemical reactions.

Semiconductor nanowire-supported palladium nanocatalysts

The design, fabrication, and surface characterisation of Pd nanoparticles supported by GaP semiconductor nanowires, investigated in **Paper III**, revealed a significant role of the support morphology of the nanocatalysts on their catalytic performance. The variation in fabrication conditions, including temperature and V/III ratio, directly

affected the resulting tapering and crystal structure of the nanowire supports. The nanocatalysts with low density and minimal tapering, characterised by a predominant wurtzite structure and extended defect-free regions near the nanowire tips, demonstrated superior catalytic activity and turnover frequency compared to their counterparts with pronounced tapering, higher density, and variations in their crystal structure. This innovative approach using pedestalled nanowires supports, paves the way for deeper exploration of the relationship between support morphology and catalytic performance, offering new opportunities for further nanocatalyst optimisation.

Nanotrees

Finally, the Pd-based nanocatalysts were further upgraded by designing and fabricating branched GaP nanowires seeded by Pd nanoparticles using Pd-seeded GaP cores nanowires, creating tree-like nanostructures, as presented in **Paper IV**. The limitations of high particle concentration leading to aggregation and broadening of the nanowire tips as well as thicker branches led to exploring other strategies, such as the use of Au-seeded GaP cores nanowires which significantly improved the branch growth. The increased surface area along with Pd-Ga phases on the branch tips, leveraged the catalytic potential of Pd particles. Further optimisation of branch design, particularly focusing on reducing kinking to achieve straighter core nanowires and branches, would enhance the overall nanostructure architecture. Additionally, refining the fabrication process would enable better control over Pd-Ga phase formation.

Outlook

The future of Pd-based nanostructures will likely focus on bridging the fundamental understanding of these nanocatalysts with specific catalytic applications. Advanced characterisation techniques will be critical in gaining deeper insights into the intricate processes of the nanocatalyst fabrication, tunning, and subsequent catalytic evaluation.

The development of more sophisticated computational models that can accurately predict nanoparticle generation will be essential. These models should incorporate multi-physics approaches to capture the complex interplay between various factors influencing the vapour plume formation and nanoparticle generation.

Furthermore, investigating the long-term stability of these complex nanostructures will be important for their practical implementation. This includes studying potential degradation mechanisms and developing strategies to enhance the durability of the nanostructures.

The principles and methodologies developed in this work can be extended to other material systems beyond Pd, Ga and GaP. Exploring a wider range of elemental combinations and support structures may lead to the discovery of novel nanoarchitectures with unique properties.

Future research could focus on exploring alternative, more cost-effective and scalable support materials. While bottom-up semiconductor synthesis offers precise control,

top-down approaches or other materials like carbon-based supports, transition metal oxides, or alloys might provide other viable paths for industrial applications.

Additionally, using the semiconductor properties of supports for photocatalytic applications presents an interesting opportunity. Although GaP might not be the optimal choice for all scenarios due to its band gap, other semiconductors or novel 2D materials could lead to more efficient photocatalytic systems.

In conclusion, this thesis lays a solid foundation for future nanostructure design and fabrication innovations. By continuing to push the boundaries of our understanding and control over nanoscale materials, we open possibilities for creating materials with tailored properties that could address critical technological challenges. Further research and development will be necessary to translate these findings into practical applications.

References

[1] K. A. Altammar, "A review on nanoparticles: characteristics, synthesis, applications, and challenges," (in eng), *Front Microbiol*, vol. 14, p. 1155622, 2023, doi: 10.3389/fmicb.2023.1155622.

[2] B. Mekuye and B. Abera, "Nanomaterials: An overview of synthesis, classification, characterization, and applications," *Nano Select*, vol. 4, no. 8, pp. 486-501, 2023, doi: 10.1002/nano.202300038.

[3] A. T. Bell, "The impact of nanoscience on heterogeneous catalysis," *Science*, vol. 299, no. 5613, pp. 1688-1691, 2003.

[4] J. J. Berzelius, *Årsberättelse om framstegen i fysik och kemi: 1835*. Norstedt, 1835.

[5] K. J. Laidler, "Chemical kinetics and the origins of physical chemistry," *Archive for History of Exact Sciences*, pp. 43-75, 1985.

[6] C. R. Catlow, M. Davidson, C. Hardacre, and G. J. Hutchings, "Catalysis making the world a better place," *Philosophical Transactions of the Royal Society A: Mathematical, Physical and Engineering Sciences*, vol. 374, no. 2061, p. 20150089, 2016, doi: 10.1098/rsta.2015.0089.

[7] E. D. Goodman, J. A. Schwalbe, and M. Cargnello, "Mechanistic Understanding and the Rational Design of Sinter-Resistant Heterogeneous Catalysts," *ACS Catalysis*, vol. 7, no. 10, pp. 7156-7173, 2017/10/06 2017, doi: 10.1021/acscatal.7b01975.

[8] J. Durand, E. Teuma, and M. Gómez, "An overview of palladium nanocatalysts: surface and molecular reactivity," *European Journal of Inorganic Chemistry*, vol. 2008, no. 23, pp. 3577-3586, 2008.

[9] M. Pérez-Lorenzo, "Palladium nanoparticles as efficient catalysts for Suzuki cross-coupling reactions," *The Journal of Physical Chemistry Letters*, vol. 3, no. 2, pp. 167-174, 2012.

[10] A. Standing *et al.*, "Efficient water reduction with gallium phosphide nanowires," *Nature Communications*, vol. 6, no. 1, p. 7824, 2015/07/17 2015, doi: 10.1038/ncomms8824.

[11] D. Kharaghani, Z. Tajbakhsh, P. D. Nam, and I. S. Kim, "Application of nanowires for retinal regeneration," *Regenerative Medicine*, p. 119, 2020.

[12] T. K. Gajaria, B. Roondhe, S. D. Dabhi, P. Śpiewak, K. J. Kurzydłowski, and P. K. Jha, "Hydrogen evolution reaction electrocatalysis trends of confined gallium phosphide with substitutional defects," *International Journal of Hydrogen Energy*, vol. 45, no. 44, pp. 23928-23936, 2020/09/07/ 2020, doi: 10.1016/j.ijhydene.2019.09.032.

[13] M. Mohammadi, "Exploring the possibility of GaPNTs as new materials for hydrogen storage," *Chinese Journal of Physics*, vol. 56, no. 4, pp. 1476-1480, 2018/08/01/ 2018, doi: 10.1016/j.cjph.2018.05.023.

[14] V. Sharov *et al.*, "Work function tailoring in gallium phosphide nanowires," *Applied Surface Science*, p. 150018, 2021.

[15] W. Hällström *et al.*, "Gallium Phosphide Nanowires as a Substrate for Cultured Neurons," *Nano Letters*, vol. 7, no. 10, pp. 2960-2965, 2007/10/01 2007, doi: 10.1021/nl070728e.

[16] C. Roth *et al.*, "Generation of Ultrafine Particles by Spark Discharging," *Aerosol Science and Technology*, Article vol. 38, no. 3, pp. 228-235, 2004, doi: 10.1080/02786820490247632.

[17] V. A. Vons, A. Anastasopol, W. J. Legerstee, F. M. Mulder, S. W. H. Eijt, and A. Schmidt-Ott, "Low-temperature hydrogen desorption and the structural properties of spark discharge generated Mg nanoparticles," *Acta Materialia*, vol. 59, no. 8, pp. 3070-3080, 2011/05/01/ 2011, doi: 10.1016/j.actamat.2011.01.047.

[18] J. H. Byeon and J. W. Kim, "Production of carbonaceous nanostructures from a silver-carbon ambient spark," *Applied Physics Letters*, Article vol. 96, no. 15, 2010, Art no. 153102, doi: 10.1063/1.3396188.

[19] A. Anastasopol, T. V. Pfeiffer, A. Schmidt-Ott, F. M. Mulder, and S. W. H. Eijt, "Fractal disperse hydrogen sorption kinetics in spark discharge generated Mg/NbOx and Mg/Pd nanocomposites," *Applied Physics Letters*, vol. 99, no. 19, 2011, doi: 10.1063/1.3659315.

[20] L. Jönsson *et al.*, "The effect of electrode composition on bimetallic AgAu nanoparticles produced by spark ablation," *Journal of Aerosol Science*, vol. 177, p. 106333, 2024/03/01/ 2024. [Online]. Available: https://www.sciencedirect.com/science/article/pii/S0021850223001982.

[21] A. Muntean, M. Wagner, J. Meyer, and M. Seipenbusch, "Generation of copper, nickel, and CuNi alloy nanoparticles by spark discharge," *Journal of Nanoparticle Research*, vol. 18, pp. 1-9, 2016.

[22] S. M. Franzén *et al.*, "Compositional tuning of gas-phase synthesized Pd–Cu nanoparticles," *Nanoscale Advances*, vol. 5, no. 22, pp. 6069-6077, 2023.

[23] A. Kohut *et al.*, "Full range tuning of the composition of Au/Ag binary nanoparticles by spark discharge generation," *Scientific reports*, vol. 11, no. 1, p. 5117, 2021.

[24] N. S. Tabrizi, Q. Xu, N. M. van der Pers, U. Lafont, and A. Schmidt-Ott, "Synthesis of mixed metallic nanoparticles by spark discharge," *Journal of Nanoparticle Research*, vol. 11, no. 5, pp. 1209-1218, 2009/07/01 2009, doi: 10.1007/s11051-008-9568-8.

[25] N. S. Tabrizi, Q. Xu, N. M. van der Pers, and A. Schmidt-Ott, "Generation of mixed metallic nanoparticles from immiscible metals by spark discharge," *Journal of Nanoparticle Research*, vol. 12, no. 1, pp. 247-259, 2010/01/01 2010, doi: 10.1007/s11051-009-9603-4.

[26] M. Armbrüster, K. Kovnir, M. Behrens, D. Teschner, Y. Grin, and R. Schlögl, "Pd-Ga intermetallic compounds as highly selective semihydrogenation catalysts," (in eng), *J Am Chem Soc*, vol. 132, no. 42, pp. 14745-7, Oct 27 2010, doi: 10.1021/ja106568t.

[27] J. Osswald *et al.*, "Structural and Catalytic Investigation of Palladium-Gallium Intermetallic Compounds," in *Hasylab Jahresbericht 2003, Annual Report*: Hamburger Synchrotronstrahlungslabor HASYLAB at Deutsches Elektronen …, 2003, pp. 443-444.

[28] M. Arzi, M. Sabzehparvar, S. K. Sadrnezhaad, and M. H. J. A. P. A. Amin, "Nanostructural study of NiTi–TiO 2–C core–shell nanoparticles generated by spark discharge method," vol. 124, no. 9, p. 625, 2018.

[29] J. H. Byeon and J. H. J. S. r. Park, "Use of aerosol route to fabricate positively charged Au/Fe 3 O 4 Janus nanoparticles as multifunctional nanoplatforms," vol. 6, no. 1, pp. 1-7, 2016.

[30] A. Schmidt-Ott, *Spark Ablation: Building Blocks for Nanotechnology*. CRC Press, 2019.

[31] N. Tabrizi, Q. Xu, N. Van Der Pers, and A. J. J. o. N. R. Schmidt-Ott, "Generation of mixed metallic nanoparticles from immiscible metals by spark discharge," vol. 12, no. 1, pp. 247-259, 2010.

[32] M. Gautam, J. O. Kim, and C. S. Yong, "Fabrication of aerosol-based nanoparticles and their applications in biomedical fields," *Journal of Pharmaceutical Investigation*, vol. 51, no. 4, pp. 361-375, 2021.

[33] G. Biskos, V. Vons, C. U. Yurteri, A. J. K. P. Schmidt-Ott, and P. Journal, "Generation and sizing of particles for aerosol-based nanotechnology," vol. 26, pp. 13-35, 2008.

[34] M. Messing, *Engineered Nanoparticles Generation, Characterization and Applications*. Lund University, 2011.

[35] M. H. Magnusson, K. Deppert, J.-O. Malm, J.-O. Bovin, and L. Samuelson, "Gold Nanoparticles: Production, Reshaping, and Thermal Charging," *Journal of Nanoparticle Research*, vol. 1, no. 2, pp. 243-251, 1999/06/01 1999, doi: 10.1023/A:1010012802415.

[36] C. R. Svensson *et al.*, "Direct Deposition of Gas Phase Generated Aerosol Gold Nanoparticles into Biological Fluids-Corona Formation and Particle Size Shifts," vol. 8, no. 9, p. e74702, 2013.

[37] B. K. Ku and A. D. J. J. o. A. S. Maynard, "Generation and investigation of airborne silver nanoparticles with specific size and morphology by homogeneous nucleation, coagulation and sintering," vol. 37, no. 4, pp. 452-470, 2006.

[38] M. H. Magnusson, K. Deppert, J.-O. Malm, J.-O. Bovin, and L. J. N. M. Samuelson, "Size-selected gold nanoparticles by aerosol technology," vol. 12, no. 1-4, pp. 45-48, 1999.

[39] M. Shimada, T. Seto, and K. J. J. o. c. e. o. J. Okuyama, "Size change of very fine silver agglomerates by sintering in a heated flow," vol. 27, no. 6, pp. 795-802, 1994.

[40] B. O. Meuller *et al.*, "Review of Spark Discharge Generators for Production of Nanoparticle Aerosols," *Aerosol Science and Technology*, vol. 46, no. 11, pp. 1256-1270, 2012/11/01 2012, doi: 10.1080/02786826.2012.705448.

[41] M. E. Messing *et al.*, "Generation of Pd Model Catalyst Nanoparticles by Spark Discharge," *The Journal of Physical Chemistry C*, vol. 114, no. 20, pp. 9257-9263, 2010/05/27 2010, doi: 10.1021/jp101390a.

[42] B. O. Meuller *et al.*, "Review of spark discharge generators for production of nanoparticle aerosols," vol. 46, no. 11, pp. 1256-1270, 2012.

[43] N. S. Tabrizi, M. Ullmann, V. Vons, U. Lafont, and A. J. J. o. N. R. Schmidt-Ott, "Generation of nanoparticles by spark discharge," vol. 11, no. 2, p. 315, 2009.

[44] R. Reinmann and M. Akram, "Temporal investigation of a fast spark discharge in chemically inert gases," *Journal of Physics D: Applied Physics*, Article vol. 30, no. 7, pp. 1125-1134, 1997, doi: 10.1088/0022-3727/30/7/010.

[45] H. Martinen and H. Tholl, "Untersuchung der Temperatur und der Expansion von Funkenkanälen in H2 bei variabler Energiezufuhr," (in English), *Zeitschrift für Naturforschung A*, vol. 25, no. 3, pp. 430-439, 01 Mar. 1970 1970, doi: 10.1515/zna-1970-0315.

[46] J. Feng *et al.*, "General Approach to the Evolution of Singlet Nanoparticles from a Rapidly Quenched Point Source," *The Journal of Physical Chemistry C*, vol. 120, no. 1, pp. 621-630, 2016/01/14 2016, doi: 10.1021/acs.jpcc.5b06503.

[47] K. E. J. Lehtinen and M. R. Zachariah, "Energy accumulation in nanoparticle collision and coalescence processes," *Journal of Aerosol Science*, vol. 33, no. 2, pp. 357-368, 2002/02/01/ 2002, doi: 10.1016/S0021-8502(01)00177-X.

[48] T. V. Pfeiffer, J. Feng, and A. Schmidt-Ott, "New developments in spark production of nanoparticles," *Advanced Powder Technology*, vol. 25, no. 1, pp. 56-70, 2014/01/01/ 2014, doi: 10.1016/j.apt.2013.12.005.

[49] W. C. Hinds, *Aerosol technology: properties, behavior, and measurement of airborne particles*, Second ed. John Wiley & Sons, 2012, pp. 320-323.

[50] C. Preger, "Magnetic-field-directed Self-assembly of Multifunctional Aerosol Nanoparticles," Ph.D. Collection of Articles, Department of Physics, Lund University, Lund, Sweden, 2020.

[51] C. Preger, N. C. Overgaard, M. E. Messing, and M. H. Magnusson, "Predicting the deposition spot radius and the nanoparticle concentration distribution in an electrostatic precipitator," *Aerosol Science and Technology*, vol. 54, no. 6, pp. 718-728, 2020.

[52] A. Balanta, C. Godard, and C. Claver, "Pd nanoparticles for C–C coupling reactions," *Chemical Society Reviews*, vol. 40, no. 10, pp. 4973-4985, 2011.

[53] V. Gryaznov *et al.*, "Palladium alloys as hydrogen permeable catalysts in hydrogenation and dehydrogenation reactions," *Journal of the Less Common Metals*, vol. 89, no. 2, pp. 529-535, 1983.

[54] N. S. Tabrizi, M. Ullmann, V. A. Vons, U. Lafont, and A. Schmidt-Ott, "Generation of nanoparticles by spark discharge," *Journal of Nanoparticle Research*, vol. 11, no. 2, p. 315, 2008/05/29 2008, doi: 10.1007/s11051-008-9407-y.

[55] D. Megyeri, A. Kohut, and Z. Geretovszky, "Effect of flow geometry on the nanoparticle output of a spark discharge generator," *Journal of Aerosol Science*, vol. 154, p. 105758, 2021/05/01/ 2021, doi: 10.1016/j.jaerosci.2021.105758.

[56] K. Han *et al.*, "A study of pin-to-plate type spark discharge generator for producing unagglomerated nanoaerosols," *Journal of Aerosol Science*, vol. 52, pp. 80-88, 2012.

[57] A. A. Efimov, V. V. Ivanov, A. V. Bagazeev, I. V. Beketov, I. A. Volkov, and S. V. Shcherbinin, "Generation of aerosol nanoparticles by the multi-spark discharge generator," *Technical Physics Letters*, vol. 39, no. 12, pp. 1053-1056, 2013/12/01 2013, doi: 10.1134/S1063785013120067.

[58] K. Deppert, M. H. Magnusson, L. Samuelson, J.-O. Malm, C. Svensson, and J.-O. Bovin, "Size-selected nanocrystals of III–V semiconductor materials by the

aerotaxy method," *Journal of Aerosol Science*, vol. 29, no. 5, pp. 737-748, 1998/06/01/ 1998. [Online]. Available: https://www.sciencedirect.com/science/article/pii/S0021850297100179.

[59] M. Snellman, "Aerosol Synthesis and Characterization of Heterogeneous Bimetallic Nanoparticles," 2023.

[60] J. Osswald *et al.*, "Palladium–gallium intermetallic compounds for the selective hydrogenation of acetylene: Part I: Preparation and structural investigation under reaction conditions," *Journal of Catalysis*, vol. 258, no. 1, pp. 210-218, 2008/08/15/ 2008, doi: 10.1016/j.jcat.2008.06.013.

[61] L. Li *et al.*, "Ga-Pd/Ga2O3 Catalysts: The Role of Gallia Polymorphs, Intermetallic Compounds, and Pretreatment Conditions on Selectivity and Stability in Different Reactions," *ChemCatChem*, vol. 4, no. 11, pp. 1764-1775, 2012. [Online]. Available: https://chemistry-europe.onlinelibrary.wiley.com/doi/abs/10.1002/cctc.201200268.

[62] S. R. Docherty and C. Copéret, "Deciphering Metal–Oxide and Metal–Metal Interplay via Surface Organometallic Chemistry: A Case Study with CO2 Hydrogenation to Methanol," *Journal of the American Chemical Society*, vol. 143, no. 18, pp. 6767-6780, 2021/05/12 2021, doi: 10.1021/jacs.1c02555.

[63] S. Penner *et al.*, "Pd/Ga2O3 methanol steam reforming catalysts: Part I. Morphology, composition and structural aspects," *Applied Catalysis A: General*, vol. 358, no. 2, pp. 193-202, 2009/05/01/ 2009. [Online]. Available: https://www.sciencedirect.com/science/article/pii/S0926860X0900132X.

[64] K. Kovnir *et al.*, "A new approach to well-defined, stable and site-isolated catalysts," *Science and Technology of Advanced Materials*, vol. 8, no. 5, p. 420, 2007/07/31 2007, doi: 10.1016/j.stam.2007.05.004.

[65] M. Krajčí and J. Hafner, "Semihydrogenation of Acetylene on the (010) Surface of GaPd2: Ga Enrichment Improves Selectivity," *The Journal of Physical Chemistry C*, vol. 118, no. 23, pp. 12285-12301, 2014/06/12 2014, doi: 10.1021/jp5025075.

[66] Z. Ye, S. Nitta, Y. Honda, M. Pristovsek, and H. Amano, "Analysis of trimethylgallium decomposition by high-resolution mass spectrometry," *Japanese Journal of Applied Physics*, vol. 59, no. 2, p. 025511, 2020/02/01 2020, doi: 10.35848/1347-4065/ab6fb0.

[67] C. A. Larsen, N. I. Buchan, S. H. Li, and G. B. Stringfellow, "Decomposition mechanisms of trimethylgallium," *Journal of Crystal Growth*, vol. 102, no. 1, pp. 103-116, 1990/04/02/ 1990. [Online]. Available: https://www.sciencedirect.com/science/article/pii/002202489090891N.

[68] B. Liu, T. Xu, C. Li, and J. Bai, "Activating Pd nanoparticles via the Mott-Schottky effect in Ni doped CeO2 nanotubes for enhanced catalytic Suzuki reaction," *Molecular Catalysis*, vol. 528, p. 112452, 2022/08/01/ 2022, doi: 10.1016/j.mcat.2022.112452.

[69] C.-H. Hao *et al.*, "Synergistic Effect of Segregated Pd and Au Nanoparticles on Semiconducting SiC for Efficient Photocatalytic Hydrogenation of Nitroarenes," *ACS Applied Materials & Interfaces*, vol. 10, no. 27, pp. 23029-23036, 2018/07/11 2018, doi: 10.1021/acsami.8b04044.

[70] S. M. Bergin, Y.-H. Chen, A. R. Rathmell, P. Charbonneau, Z.-Y. Li, and B. J. Wiley, "The effect of nanowire length and diameter on the properties of transparent, conducting nanowire films," *Nanoscale*, 10.1039/C2NR30126A vol. 4, no. 6, pp. 1996-2004, 2012, doi: 10.1039/C2NR30126A.

[71] E. Givargizov, "Fundamental aspects of VLS growth," in *Vapour Growth and Epitaxy*: Elsevier, 1975, pp. 20-30.

[72] B. A. Wacaser, K. A. Dick, J. Johansson, M. T. Borgström, K. Deppert, and L. Samuelson, "Preferential Interface Nucleation: An Expansion of the VLS Growth Mechanism for Nanowires," *Advanced Materials*, vol. 21, no. 2, pp. 153-165, 2009, doi: 10.1002/adma.200800440.

[73] V. G. Dubrovskii and F. Glas, "Vapor–Liquid–Solid Growth of Semiconductor Nanowires," in *Fundamental Properties of Semiconductor Nanowires*, N. Fukata and R. Rurali Eds. Singapore: Springer Singapore, 2021, pp. 3-107.

[74] K. Hillerich, K. A. Dick, M. E. Messing, K. Deppert, and J. Johansson, "Simultaneous growth mechanisms for Cu-seeded InP nanowires," *Nano Research*, vol. 5, no. 5, pp. 297-306, 2012/05/01 2012, doi: 10.1007/s12274-012-0210-9.

[75] D. E. Perea, N. Li, R. M. Dickerson, A. Misra, and S. T. Picraux, "Controlling Heterojunction Abruptness in VLS-Grown Semiconductor Nanowires via in situ Catalyst Alloying," *Nano Letters*, vol. 11, no. 8, pp. 3117-3122, 2011/08/10 2011, doi: 10.1021/nl201124y.

[76] G. Meng *et al.*, "A flux induced crystal phase transition in the vapor–liquid–solid growth of indium-tin oxide nanowires," *Nanoscale*, 10.1039/C4NR01016G vol. 6, no. 12, pp. 7033-7038, 2014, doi: 10.1039/C4NR01016G.

[77] H. Cui, Y. Y. Lü, G. W. Yang, Y. M. Chen, and C. X. Wang, "Step-Flow Kinetics Model for the Vapor–Solid–Solid Si Nanowires Growth," *Nano Letters*, vol. 15, no. 5, pp. 3640-3645, 2015/05/13 2015, doi: 10.1021/acs.nanolett.5b01442.

[78] T. Hu *et al.*, "In Situ Manipulation of Growth Mechanisms in the Vapor–Solid–Solid Growth of GaP Nanowires," *Advanced Materials Interfaces*, vol. n/a, no. n/a, p. 2400805, doi: 10.1002/admi.202400805.

[79] C. B. Maliakkal, M. Tornberg, D. Jacobsson, S. Lehmann, and K. A. Dick, "Vapor–solid–solid growth dynamics in GaAs nanowires," *Nanoscale Advances*, vol. 3, no. 20, pp. 5928-5940, 2021.

[80] S. V. Thombare, A. F. Marshall, and P. C. McIntyre, "Size effects in vapor-solid-solid Ge nanowire growth with a Ni-based catalyst," *Journal of Applied Physics*, vol. 112, no. 5, p. 054325, 2012, doi: 10.1063/1.4749797.

[81] S. Franzén, "Design and development of solid-state nanostructures for catalysis," 2023.

[82] S. Lehmann, J. Wallentin, D. Jacobsson, K. Deppert, and K. A. Dick, "A General Approach for Sharp Crystal Phase Switching in InAs, GaAs, InP, and GaP Nanowires Using Only Group V Flow," *Nano Letters*, vol. 13, no. 9, pp. 4099-4105, 2013/09/11 2013, doi: 10.1021/nl401554w.

[83] L. S. KARLSSON *et al.*, "CRYSTAL STRUCTURE OF BRANCHED EPITAXIAL III–V NANOTREES," *Nano*, vol. 01, no. 02, pp. 139-151, 2006, doi: 10.1142/s1793292006000203.

[84] K. A. Dick *et al.*, "Synthesis of branched 'nanotrees' by controlled seeding of multiple branching events," *Nature Materials*, vol. 3, no. 6, pp. 380-384, 2004/06/01 2004, doi: 10.1038/nmat1133.

[85] J. Osswald *et al.*, "Palladium–gallium intermetallic compounds for the selective hydrogenation of acetylene: Part II: Surface characterization and catalytic performance," *Journal of Catalysis*, vol. 258, no. 1, pp. 219-227, 2008/08/15/ 2008, doi: 10.1016/j.jcat.2008.06.014.

[86] R. N. Wenzel, "Resistance of solid surfaces to wetting by water," *Industrial & engineering chemistry*, vol. 28, no. 8, pp. 988-994, 1936.

[87] A. Cassie and S. Baxter, "Wettability of porous surfaces," *Transactions of the Faraday society*, vol. 40, pp. 546-551, 1944.

[88] A. Cassie, "Contact angles," *Discussions of the Faraday society*, vol. 3, pp. 11-16, 1948.

[89] R. A. Basimova *et al.*, "Selective hydrogenation on palladium-containing catalysts of byproduct phenylacetylene present in industrial fractions of styrene," *Petroleum Chemistry*, vol. 49, no. 5, pp. 360-365, 2009/09/01 2009, doi: 10.1134/S096554410905003X.

[90] X. Li, R. Wang, J. Zhang, J. Wang, Y. Wang, and Z. Zheng, "Selective hydrogenation of phenylacetylene over TiO 2 supported Ni 2 P nanoparticles under visible light irradiation," *Catalysis Science & Technology*, vol. 13, no. 22, pp. 6519-6526, 2023.

[91] S. Kozuch and J. M. L. Martin, ""“Turning Over” Definitions in Catalytic Cycles," *ACS Catalysis*, vol. 2, no. 12, pp. 2787-2794, 2012/12/07 2012, doi: 10.1021/cs3005264.

[92] H. Lindlar and R. Dubuis, "Palladium catalyst for partial reduction of acetylenes," *Organic Syntheses*, vol. 5, p. 880, 1973.

[93] C. Trento, "Utilizing Catalyst Poisoning to Improve Catalyst Selectivity: The Role of Lindlar Catalysts." [Online]. Available: https://www.samaterials.com/content/catalyst-poisoning-to-improve-selectivity-lindlar-catalysts.html.

[94] M. J. Maccarrone *et al.*, "Nanoparticles of tungsten as low-cost monometallic catalyst for selective hydrogenation of 3-hexyne," *Química Nova*, vol. 39, pp. 1-8, 2016.

[95] M. Zhang *et al.*, "Highly selective semihydrogenation via a wettability-regulated mass transfer process," *ACS Catalysis*, vol. 12, no. 14, pp. 8494-8502, 2022.

Appendix A

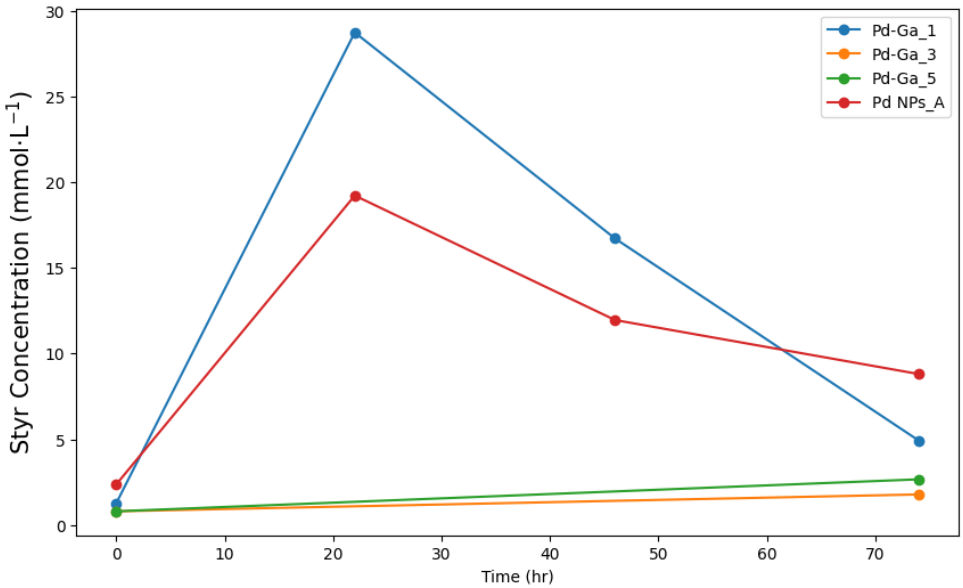

Figure A1 Styrene (Styr) formation over time for Pd-based nanocatalysts, *during a partial hydrogenation reaction of* phenylacetylene (PA) *to Styr.*

Appendix B

A brief description of the following characterisation techniques used in Papers II, III, and IV, as well as in this thesis, is included in this section.

Scanning Electron Microscope (SEM):

The SEM uses a focused beam of electrons to scan the surface of a sample. As the beam interacts with the specimen, it generates various signals, including secondary and backscattered electrons. These electrons are collected by detectors and used to create a high-resolution image of the sample's surface topography. An electron gun produces the electron beam and focuses on the sample using electromagnetic lenses. The beam is scanned across the sample surface in a raster pattern, and the detected signals are used to build up the image pixel by pixel. SEMs can achieve magnifications up to 500,000x and resolutions down to a few nanometres.

Transmission Electron Microscope (TEM):

The TEM operates by transmitting a beam of electrons through an ultra-thin specimen. As the electrons pass through the sample, they interact with its internal structure, creating a 2D image. The electron beam is generated by an electron gun and focused using electromagnetic lenses. The transmitted electrons are then projected onto a fluorescent screen or detected by a camera to form the image. TEMs can achieve much higher magnifications and resolutions than SEMs, allowing for the visualisation of atomic-scale structures. The specimen preparation for TEM is critical, as samples must be thin enough (typically less than 100 nm) to allow electrons to pass through.

Energy-dispersive X-ray Spectroscopy (EDX):

EDX is an analytical technique often used in conjunction with electron microscopes (SEM and TEM). It relies on the principle that each element has a unique atomic structure, producing characteristic X-rays when excited by high-energy particles. In an electron microscope, the incident electron beam excites electrons in the sample's atoms, causing them to emit X-rays. An EDX detector collects these X-rays and analyses their energy spectrum. This allows for the identification and quantification of elements present in the sample. EDX can provide information about the elemental composition of a specimen with spatial resolution.

Scanning Transmission Electron Microscope (STEM):

STEM combines principles of both SEM and TEM. It uses a focused electron beam that is scanned across a thin sample, similar to SEM, but the electrons that pass through the sample are collected to form an image, as in TEM. STEM offers several advantages, including the ability to perform simultaneous imaging and spectroscopy. It can achieve atomic resolution and is particularly useful for analysing the composition and structure

of materials at the nanoscale. STEM is often used in conjunction with techniques like EDX for detailed elemental analysis.

High-angle Annular Dark-field Imaging (HAADF):

HAADF is an imaging technique used in STEM. It collects electrons that are scattered at high angles (typically >50 mrad) by the sample. These high-angle scattered electrons are primarily due to Rutherford scattering, which is strongly dependent on the atomic number of the scattering atoms. As a result, HAADF images provide strong atomic number (Z) contrast, with heavier elements appearing brighter. This makes HAADF particularly useful for imaging materials with varying compositions, as it can clearly distinguish between elements of different atomic numbers.

X-ray Photoelectron Spectroscopy (XPS):

XPS is a surface-sensitive spectroscopic technique used to analyse the elemental composition, chemical state, and electronic state of elements within a material. It works by irradiating a sample with X-rays and measuring the kinetic energy and number of electrons that escape from the top 1-10 nm of the material's surface. Each element produces a characteristic set of XPS peaks at specific binding energy values. The position and intensity of these peaks can provide information about the chemical environment of the atoms. XPS is widely used in materials science and surface chemistry to analyse surface compositions, study chemical bonding, and investigate surface modifications.